Available online at www.sciencedirect.com
SCIENCE DIRECT®
International Journal of Heat and Mass Transfer 48 (2005) 4410–4427
International Journal of HEAT and MASS TRANSFER
www.elsevier.com/locate/ijhmt

Constructal PEM fuel cell stack design

J.V.C. Vargas [a,*], J.C. Ordonez [b], A. Bejan [c]

[a] Departamento de Engenharia Mecânica, Universidade Federal do Paraná, C.P. 19011, Curitiba, Paraná 81531-990, Brazil
[b] Department of Mechanical Engineering and Center for Advanced Power Systems, Florida State University, Tallahassee, FL 32310-6046, USA
[c] Department of Mechanical Engineering and Materials Science, Duke University, Durham, NC 27708-0300, USA

Received 8 March 2005; received in revised form 12 May 2005
Available online 14 July 2005

Abstract

This paper describes a structured procedure to optimize the internal structure (relative sizes, spacings), single cells thickness, and external shape (aspect ratios) of a polymer electrolyte membrane fuel cell (PEMFC) stack so that net power is maximized. The constructal design starts from the smallest (elemental) level of a fuel cell stack (the single PEMFC), which is modeled as a unidirectional flow system, proceeding to the pressure drops experienced in the headers and gas channels of the single cells in the stack. The polarization curve, total and net power, and efficiencies are obtained as functions of temperature, pressure, geometry and operating parameters. The optimization is subjected to fixed stack total volume. There are two levels of optimization: (i) the internal structure, which accounts for the relative thicknesses of two reaction and diffusion layers and the membrane space, together with the single cells thickness, and (ii) the external shape, which accounts for the external aspect ratios of the PEMFC stack. The flow components are distributed optimally through the available volume so that the PEMFC stack net power is maximized. Numerical results show that the optimized single cells internal structure and stack external shape are "robust" with respect to changes in stoichiometric ratios, membrane water content, and total stack volume. The optimized internal structure and single cells thickness, and the stack external shape are results of an optimal balance between electrical power output and pumping power required to supply fuel and oxidant to the fuel cell through the stack headers and single-cell gas channels. It is shown that the twice maximized stack net power increases monotonically with total volume raised to the power 3/4, similarly to metabolic rate and body size in animal design.

Keywords: Constructal; Fuel cells; PEMFC structure; Fuel cell thickness; Shape

1. Introduction

The world currently relies almost entirely on fossil fuels to supply its energy needs. In the near future, it is expected that the world's fossil fuel reserves will not meet the growing energy demand. To reduce dependence on oil, the world's most developed nations have been investing in cutting edge research to develop sustainable

* Corresponding author. Tel.: +55 41 361 3307; fax: +55 41 361 3129.
E-mail addresses: jvargas@demec.ufpr.br (J.V.C. Vargas), ordonez@eng.fsu.edu (J.C. Ordonez), dalford@duke.edu (A. Bejan).

0017-9310/$ - see front matter © 2005 Elsevier Ltd. All rights reserved.
doi:10.1016/j.ijheatmasstransfer.2005.05.009

Nomenclature

A	area, m^2
A_c	total gas channel cross-sectional area, m^2
A_{ch}	headers cross-sectional area, m^2
A_s	unit fuel cell cross-sectional area, m^2
$\widetilde{A}$	dimensionless area
B	dimensionless constant
c	specific heat, kJ kg^{-1} K^{-1}
c_p	specific heat at constant pressure, kJ kg^{-1} K^{-1}
c_v	specific heat at constant volume, kJ kg^{-1} K^{-1}
C	constant
CV	control volume
D	Knudsen diffusion coefficient, m^2 s^{-1}
E	dimensionless conversion factor, Eq. (32)
D_h	gas channel hydraulic diameter, m
f	friction factor
F	Faraday constant, 96,500 C eq^{-1}
h	heat transfer coefficient, W m^{-2} K^{-1}
$\tilde{h}$	dimensionless heat transfer coefficient
$H_i(T_i)$	molar enthalpy of formation at a temperature T_i of reactants and products, kJ $kmol^{-1}$ of compound i
$\widetilde{H}_i(\theta_i)$	dimensionless molar enthalpy of formation at a dimensionless temperature θ_i of reactants and products
$i_{o,a}$, $i_{o,c}$	exchange current densities, A m^{-2}
$i_{Lim,a}$, $i_{Lim,c}$	limiting current densities, A m^{-2}
I	current, A
$\widetilde{I}$	dimensionless current
j	mass flux, kg s^{-1} m^{-2}
k	thermal conductivity, W m^{-1} K^{-1}
K	permeability, m^2
K_{bc}	bending-contraction coefficient
K_{be}	bending-expansion coefficient
$\tilde{k}$	dimensionless thermal conductivity
L	length, m
L_c, L_t	gas channels internal dimensions as shown in Fig. 1, m
L_x, L_y, L_z	stack length, width and height, respectively, m
$\dot{m}$	mass flow rate, kg s^{-1}
M	molecular weight, kg $kmol^{-1}$
n	equivalent electron per mole of reactant, eq mol^{-1}
$\dot{n}$	molar flow rate, kmol s^{-1}
n_c	number of parallel ducts in gas channel
n_s	number of single cells in the stack
N	dimensionless global wall heat transfer coefficient
p	pressure, N m^{-2}
$\tilde{p}_s$	perimeter of cross-section, m
P	dimensionless pressure
PEMFC	polymer electrolyte membrane fuel cell
Pr	Prandtl number, $\mu c_p/k$
q	tortuosity
Q	reaction quotient
$\dot{Q}$	heat transfer rate, W
$\widetilde{Q}$	dimensionless heat transfer rate
r	pore radius, m
R	ideal gas constant, kJ kg^{-1} K^{-1}
$\overline{R}$	universal gas constant, 8.314 kJ $kmol^{-1}$ K^{-1}
Re_{D_h}	Reynolds number based on D_h, $uD_h\rho/\mu$
S	dimensionless conversion factor
t	time, s
T	temperature, K
u	mean velocity, m s^{-1}
$\tilde{u}$	dimensionless mean velocity
U	global wall heat transfer coefficient, W m^{-2} K^{-1}
V	electrical potential, V
V_T	total volume, m^3
$\widetilde{V}$	dimensionless electrical potential
$\widetilde{V}_T$	dimensionless total volume
W	electrical work, J
$\widetilde{W}$	dimensionless required pumping power in the headers, Eq. (29)
$\widetilde{W}_{net}$	dimensionless PEMFC stack net power, Eq. (30)
$\widetilde{W}_{net,s}$	dimensionless single PEMFC net power
$\widetilde{W}_p$	dimensionless required single PEMFC pumping power
$\widetilde{W}_s$	dimensionless single PEMFC total electrical power
x	axial direction, Fig. 2
$y_{2,4,6}$	size constraints
[ ]	molar concentration of a substance, mol l^{-1}

Greek symbols

α_a, α_c	anode and cathode charge transfer coefficients
β	electrical resistance, Ω
γ	ratio of specific heats
δ	gas channel aspect ratio
ΔG	molar Gibbs free energy change, kJ $kmol^{-1}$ H_2, Eq. (9)
$\Delta\widetilde{G}$	dimensionless Gibbs free energy change
ΔH	molar enthalpy change, kJ $kmol^{-1}$ H_2
$\Delta\widetilde{H}$	dimensionless enthalpy change
ΔS	molar entropy change, kJ $kmol^{-1}$ K^{-1}
ζ	stoichiometric ratio
η_a, η_c	anode and cathode charge transfer overpotentials, V
$\eta_{d,a}$, $\eta_{d,c}$	anode and cathode mass diffusion overpotentials, V

η_i	ideal efficiency, Eq. (31)
η_I	first law efficiency, Eq. (32)
η_{II}	second law efficiency, Eq. (33)
η_{net}	PEMFC stack net efficiency, Eq. (34)
$\tilde{\eta}_a$, $\tilde{\eta}_c$	dimensionless anode and cathode charge transfer overpotentials
$\tilde{\eta}_{d,a}$, $\tilde{\eta}_{d,c}$	dimensionless anode and cathode mass diffusion overpotentials
$\tilde{\eta}_{ohm}$	dimensionless fuel cell total ohmic potential loss, Eq. (18)
θ	dimensionless temperature
λ	ionomer water content
μ	viscosity, Pa s
v_i	reaction coefficients
ξ	dimensionless length
ρ	density, kg m^{-3}
$\tilde{\rho}$	dimensionless density
σ	electrical conductivity, Ω^{-1} m^{-1}
τ	dimensionless time
ϕ	porosity
ψ	dimensionless mass flow rate

Subscripts

a	anode
(aq)	aqueous solution
c	cathode
e	reversible
f	fuel
(g)	gaseous phase
h	header cross-section horizontal side
$h_{f,in}$	input fuel header
$h_{f,out}$	output fuel header
$h_{ox,in}$	input oxidant header
$h_{ox,out}$	output oxidant header
H^+	hydrogen cation
H_2	hydrogen
H_2O	water produced in a single PEMFC
i	irreversible
i, a	irreversible at the anode
i, c	irreversible at the cathode
in	inlet
Lim	limiting condition
(l)	liquid phase
m	maximum with respect to fuel cell internal structure and cell thickness
mm	maximum with respect to PEMFC internal structure, cell thickness and external shape
ohm	ohmic
opt	optimal value
out	outlet
ox	oxidant
O_2	oxygen
pm	polymer electrolyte membrane
ref	reference level
s	single PEMFC
s, a	anode solid side
s, c	cathode solid side
v	header cross-section vertical side
w	wall
wa	water
wet	wetted surface
0	initial condition
1,...,7	control volumes, Fig. 2
ij	interaction between CV*i* and CV*j* ($i,j = 1,\ldots,7$)
∞	ambient

Superscript

∘	standard conditions [gases at 1 atm, 25 °C, species in solution at 1 M, where M is the molarity = (moles solute)/(liters solution)]

alternative energy sources such as fusion, and to employ hydrogen produced from diverse sources. The energy engineering community is expected to play an important role in this first international attempt to limit atmospheric pollution (in particular, to reduce the emission of greenhouse gases). To this end, polymer electrolyte membrane fuel cells (PEMFC) offer an attractive and environmentally friendly on-site alternative power generation technology, which is highly efficient, and has stationary and mobile applications [1–3].

The commercial development of PEMFC still has serious technical and economic hurdles to overcome. A practical fuel cell system requires the integration of the stack with fuel processing, heat exchange, power conditioning, and control systems. Considerable research has been conducted on new and advanced materials to lower the precious material load in the catalyst layers, membrane improvement, and on the multiple internal physical and electrochemical aspects of a single PEMFC. During the last two decades, such efforts have reduced the energy cost of PEMFC from US$4500/kW to US$1200/kW, which is still far from the energy cost (US$20/kW) of internal combustion engines [1,2]. At the PEMFC stack level, suitable materials have been developed for making small and light weight components [4], high power density electrodes to reduce the total numbers and sizes of cells and bipolar plates [4,5]. Furthermore, light weight metal conductive elements together with nonconductive elements fabricated from engineering thermoplastics were used to yield light weight and low cost PEMFC stacks [6]. Alternative materials and design concepts were presented by Kumar

and Reddy [7] for the bipolar/end plate of PEMFC stacks, which is one of the most important and costliest stack components and accounts for more than 80% of the total weight of the stack. Therefore, one direction to be pursued to make PEMFC systems competitive economically with other existing power and vehicular systems is system optimization at the stack level.

The PEMFC stack is a combination of several flow systems, i.e., electrical, chemical, fluid and heat flows. The optimization of flow-system architecture is common in engineering and nature. Constructal theory [8] is the thought that geometry (flow architecture) is generated by the pursuit of global performance subject to global constraints, in flow systems the geometry of which is free to vary. According to constructal theory, the optimization of flow architecture starts at the smallest (elemental) scale, in this case, the single PEMFC. Irreversibilities due to pressure drops, charge transfer, electrical resistances, and mass diffusion are minimized together for maximum global performance at the stack level. The technique proposed in this paper traces the general direction of flow geometry optimization subject to global constraints (e.g., volume), with the objective of maximizing the PEMFC stack net power or the net power density. This approach is general because it may be used in conjunction with other methods of improvement discussed in the previous paragraph.

The technical literature shows several previous PEMFC analytical and numerical models. At the single PEMFC level, models considering one or two-dimensional geometry, isothermal and steady state operation [9–15], and three-dimensional steady state [16] were developed. The two- and three-dimensional models are not suitable for the optimization of flow geometry, because for a PEMFC stack they would require the solving of partial differential equations for flow simulation in a very large number of flow configurations. At the PEMFC stack level, Amphlett et al. [17] introduced a transient mathematical model for predicting the response and performance of the system for applications where the operating conditions change with time, considering heat losses, changes in stack temperature, reactant gas concentrations, and other internal phenomena, but no consideration was given to the pressure drops experienced by the fuel and oxidant in the feeding headers and gas channels. Experimental results were presented by Hamelin et al. [18] for the time response of a stationary PEMFC stack under fast load commutations, and compared to the Amphlett et al. [17] model with good agreement. Several other experimental studies have been conducted to access the dynamic behavior of PEMFC stacks in search for performance improvement in the transient mode [19–23]. Recent studies presented PEMFC stack steady state mathematical models to predict performance [24–26]: one study [26] presented a genetic algorithm technique for finding the best configuration of the stack in terms of number of cells and cell surface area, but did not consider headers and gas channels pumping power losses. No transient model was found in the literature that addresses the spatial temperature and pressure gradients in a PEMFC stack, pressure drops in the headers and single cells gas channels and their effect on performance.

This study proposes a new integrative framework for the energy-based design of PEMFC stacks. The approach is cross-disciplinary and pursues simultaneously (i) the *local* optimization of components and processes with (ii) the optimal *global* integration and configuration of the system. The constructal approach chosen in this paper was introduced in previous studies for a single alkaline fuel cell [27] and for a single PEMFC [28], which divides the single fuel cell into several control volumes that correspond to the most representative parts of the flow system. For the PEMFC stack, the single cell model is extended for predicting unsteady state operation, and the stack input and output headers pressure drops are accounted for. The model is represented by a system of ordinary differential equations with respect to time, the solution of which consists of the temperatures and pressures of each control volume, and the polarization and net power curves for the PEMFC stack. The model is simple enough to insure small computational time requirements, so that it is possible to simulate the flow in a very large number of competing flow configurations.

2. Mathematical model

A PEMFC stack is shown schematically in Fig. 1. The stack is fed by two input headers, one carries fuel and the other oxidant, which are delivered to each single PEM fuel cell in the stack. After the fuel and oxidant streams sweep the single PEMFC gas channels in the stack, two output headers collect the used gases and the water that is produced by the reactions in the fuel cells. Electrical power is produced by the stack, and a fraction is used to pump the fuel and oxidant across the PEMFC stack, through the input and output headers, and through very narrow gas channels in each single fuel cell. For simplicity, the model is based on the assumption that the fuel stream is pure hydrogen, and that the oxidant is pure oxygen.

A single PEMFC is divided into seven control volumes that interact energetically with one another. In the present model, it is assumed the existence of a cooling channels system that irrigates the bipolar plates, and that the cooling fluid (e.g., water, air) is kept at an average specified temperature, T_∞, between single cells and around the stack. In this way, the electrical power delivered by the entire stack results from the analysis of one single cell, i.e., the electrical power produced by the

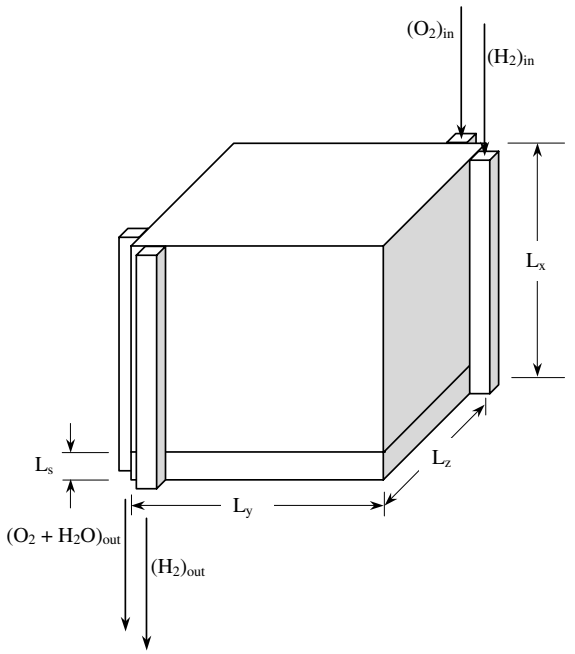

Fig. 1. The configuration of a PEMFC stack.

stack is the electrical power produced by a single cell multiplied by the number of cells in the stack, which is a variable in the PEMFC stack constructal design procedure. However, the required pumping power depends on the flow structure of the entire PEMFC stack.

The mathematical model for a single cell operating at steady state was introduced in a previous study by Vargas et al. [28]. In this paper, the mathematical model is extended for the unsteady state to predict the fuel cell stack start up time, and for possible future control and real time operation purposes. For that, the model equations are rederived with the inclusion of the thermal inertia terms for each fuel cell compartment.

Fig. 2 shows schematically the division of a single PEMFC into seven control volumes. In addition, there are two bipolar plates (interconnects) that have the function of allowing the electrons produced by the electrochemical oxidation reaction at the anode to flow to the external circuit or to an adjacent cell. The control volumes (CV) are the fuel channel (CV1), the anode diffusion backing layer (CV2), the anode reaction layer (CV3), the polymer electrolyte membrane (CV4), the cathode reaction layer (CV5), the cathode diffusion backing layer (CV6) and the oxidant channel (CV7).

The model consists of the complete conservation equations for each control volume, and the equations accounting for electrochemical reactions. The reversible electrical potential and power of the fuel cell are then computed (based on the reactions) as functions of the temperature and pressure fields determined by the model. The instantaneous electrical potential and power of the fuel cell are obtained as functions of each compartment temperature, by subtracting from the reversible potential the losses due to surface overpotentials (poor electrocatalysis), slow diffusion and internal ohmic losses through the cell (resistance of individual cell components, including electrolyte membrane, bipolar plates, interconnects and any other cell components through which electrons flow). These are functions of the total cell current (I), which is directly related to the external load (or the cell voltage), and time. In sum, the total cell current and time are considered the independent variables. The following analysis is therefore for unsteady state fuel cell operation.

The hydrogen mass flow rate required by a single PEMFC in the stack for the current (I) dictated by the external load is

$$\dot{m}_{H_2} = \dot{n}_{H_2} M_{H_2} = \frac{I}{nF} M_{H_2} \tag{1}$$

where $\dot{n}_i$ is the molar flow rate for species i, M_i the molecular weight of species i, n the number of moles of electrons formed in the reaction and F the Faraday constant, 96,500 C eq^{-1}. Accordingly, the oxygen mass flow rate needed for a single PEMFC in the stack is $\dot{m}_{O_2} = \dot{n}_{H_2} M_{O_2}$.

Nondimensional variables are defined based on the geometric and operating parameters of the system. Pressures are referenced to ambient conditions: $P_i = p_i/p_\infty$, and temperatures referenced to the specified coolant (e.g., water, air) average temperature: $\theta_i = T_i/T_\infty$.

The total volume of the fuel cell stack, $V_T = L_x L_y L_z$, is finite and fixed. This is a realistic design constraint, which accounts for the finiteness of the available space and the general push for doing the most with limited resources. The maximization of performance for the specified volume means the maximization of performance *density*. The fixed length scale $V_T^{1/3}$ is used to nondimensionalize all the lengths of the fuel cell stack geometry. Also, for presenting dimensionless results and recognizing the fuel cell net power varies with size V_T, a dimensionless fuel cell total volume is defined. The dimensionless lengths and total volume are written as

$$\xi_j = \frac{L_j}{V_T^{1/3}}, \quad \widetilde{V}_T = \frac{V_T}{V_{T,ref}} \tag{2}$$

where the subscript j indicates a particular dimension of the fuel cell stack geometry, Figs. 1 and 2, and $V_{T,ref}$ is a reference volume. Additional dimensionless variables are defined as

$$\psi_i = \frac{\dot{m}_i}{\dot{m}_{ref}}, \quad N_i = \frac{U_{wi} V_T^{2/3}}{\dot{m}_{ref} c_{p,f}}, \quad \widetilde{A}_i = \frac{A_i}{V_T^{2/3}},$$
$$\gamma_i = \frac{c_{p,i}}{c_{v,i}}, \quad \tau = \frac{t}{t_{ref}} \tag{3}$$

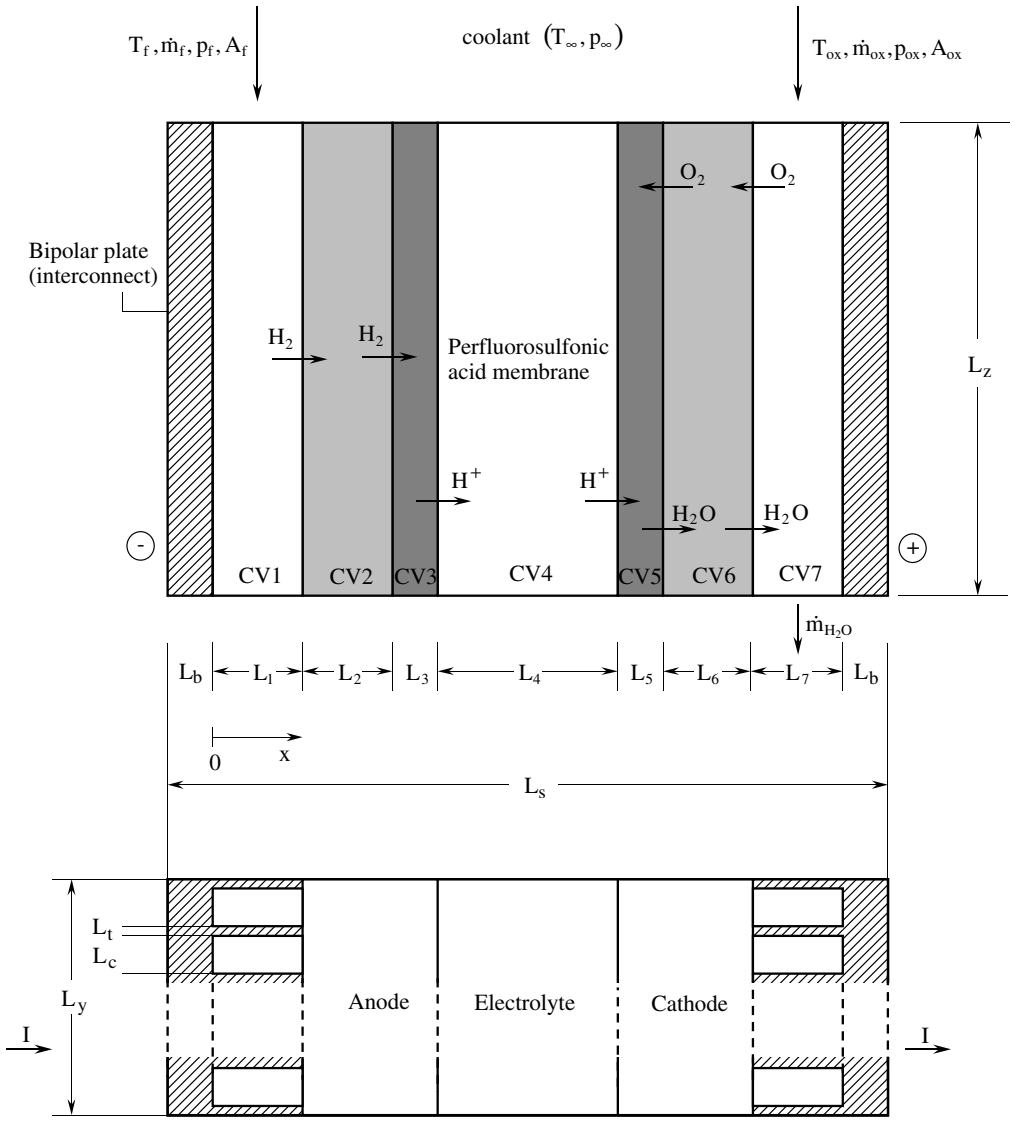

Fig. 2. The internal structure of a single PEMFC.

where subscript i indicates a substance or a location in the fuel cell, $\dot{m}_{\mathrm{ref}} = p_\infty V_{\mathrm{T}}/(R_{\mathrm{f}} T_\infty t_{\mathrm{ref}})$ is a reference mass flow rate, and R_{f} is the ideal gas constant of the fuel, N is the dimensionless global wall heat transfer coefficient, $\widetilde{A}$ is the dimensionless area, γ is the ratio of specific heats, $c_{p,i}$ and $c_{v,i}$ are the specific heats at constant pressure and volume of substance i, respectively, and t_{ref} is a specified reference time.

In a single fuel cell shown in Fig. 2, the wall heat transfer area of one control volume is $A_{\mathrm{w}i} = \tilde{p}_{\mathrm{s}} L_i$ $(2 \leqslant i \leqslant 6)$ and $A_{\mathrm{w}i} \cong \tilde{p}_{\mathrm{s}} L_i + L_y L_z$ $(i = 1, 7$; assuming that $L_{\mathrm{t}} \ll L_{\mathrm{c}}$ in Fig. 2), where $\tilde{p}_{\mathrm{s}} = 2(L_y + L_z)$ is the perimeter of the fuel cell cross-section. The control volumes are $V_j = L_y L_z L_j$ $(2 \leqslant j \leqslant 6)$ and $V_j = n_{\mathrm{c}} L_{\mathrm{c}} L_j L_z$ $(j = 1, 7)$, where n_{c} is the integer part of $L_y/(L_{\mathrm{t}} + L_{\mathrm{c}})$, i.e., the number of parallel ducts in each gas channel (fuel and oxidant).

The average fuel pressure (p_{f} in headers and CV1) and oxidant pressure (p_{ox} in headers and CV7) are assumed known and constant during fuel cell operation. The stoichiometric ratio for an electrode reaction is defined as the provided reactant (moles/s) divided by the reactant needed for the electrochemical reaction of interest. In the present model, stoichiometric ratios greater than 1 are prescribed on the fuel side (ζ_1) and oxidant side (ζ_7). The mass and energy balances for incompressible flow yield the temperature in CV1,

$$\frac{d\theta_1}{d\tau} = \left[\widetilde{Q}_{w1} + \psi_f(\theta_f - \theta_1) + \widetilde{Q}_{12} + \widetilde{Q}_{1ohm}\right] \frac{\theta_{1,0}\gamma_f}{P_f n_c \xi_1 \xi_c \xi_z} \tag{4}$$

where $\theta_{1,0}$ is a specified initial condition, $\psi_f = \zeta_1 \psi_{H_2}$, $\widetilde{Q}_{wi} = N_i \widetilde{A}_{wi}(1-\theta_i)$, where subscript i refers to one of the control volumes, $\widetilde{Q}_{12} = \tilde{h}_1 \widetilde{A}_s(1-\phi_2)(\theta_2-\theta_1)$, $\tilde{h}_1 = h_1 V_T^{2/3}/(\dot{m}_{ref} c_{p,f})$, ϕ_i are the porosities, and $\widetilde{A}_s = L_y L_z / V_T^{2/3}$ is the dimensionless cross-sectional area of the fuel cell. The dimensionless heat transfer rates for all the compartments are $\widetilde{Q}_i = \dot{Q}_i/(\dot{m}_{ref} c_{p,f} T_\infty)$, where i accounts for any of the heat transfer interactions that are present in the model. The ohmic heating is $\widetilde{Q}_{iohm} = I^2 \beta_i/(\dot{m}_{ref} c_{p,f} T_\infty)$, where subscript i refers to a control volume (1–7), and β (Ω) is the electrical resistance.

Next is the anode backing diffusion layer (CV2), where reactions are absent. Both electrodes in a fuel cell are porous, such that a large surface area can be obtained to provide good contact between the electrode and the electrolyte (ionomer). Although the porous medium consists of a solid side and a fluid side, the mass of fluid in CV2 is negligible relative to the mass of solid, therefore only the solid is taken into account in the energy balance. The net heat transfer rates are $\widetilde{Q}_2 = -\widetilde{Q}_{12} + \widetilde{Q}_{w2} + \widetilde{Q}_{23} + \widetilde{Q}_{2ohm}$, where $\widetilde{Q}_{23} = -\widetilde{k}_{s,a}(1-\phi_2) \times \widetilde{A}_s(\theta_2-\theta_3)/[(\xi_2+\xi_3)/2]$. The dimensionless thermal conductivity is defined by $\widetilde{k}_i = k_i V_T^{1/3}/(\dot{m}_{ref} c_{p,f})$.

The contact areas in the porous anode and cathode are estimated by assuming dual-porosity electrodes. The pores are approximated as parallel tubes with an average diameter of the same order as the square root of the porous medium permeability, $K^{1/2}$. Therefore, the contact (wetted) area for each porous control volume is $A_{j,wet} = 4\phi_j L_j K_j^{-1/2} A_s$, where K_j are the permeabilities.

Diffusion is assumed to be the dominant transport mechanism across the diffusion and catalyst layers. For Knudsen flow, the fuel and oxidant mass fluxes in the porous layers are given by [29]

$$j_i = -[D(\rho_{out} - \rho_{in})/L]_i, \quad i = 2, 6 \tag{5}$$

where $D = B\{r[8\overline{R}T/(\pi M)]^{1/2}\phi^q\}$ is the Knudsen diffusion coefficient, ρ the density, $\overline{R}$ the universal gas constant, ϕ the porosity, q the tortuosity [30,31], and B is a correction coefficient. By using Eq. (5) and the ideal gas model for H_2 and O_2, the pressures of the hydrogen and oxygen that enter the catalyst layers are calculated from

$$P_{i,out} = P_{i,in} - \frac{j_i R_i T_\infty L_i \theta_i}{D_i p_\infty}, \quad i = 2, 6 \tag{6}$$

where $j_2 = \dot{m}_{H_2}/A_{3,wet}$ and $j_6 = \dot{m}_{O_2}/A_{5,wet}$, and $A_{3,wet}$ and $A_{5,wet}$ are the wetted areas in the porous catalyst layers. Note also that $P_{2,in} = P_f$ and $P_{6,in} = P_{ox}$. The average pressures in CV2 and CV6 are estimated as $P_i = \frac{1}{2}(P_{i,in} + P_{i,out})$, $i = 2, 6$.

The energy balance delivers the CV2 temperature,

$$\frac{d\theta_2}{d\tau} = \left[\theta_1 - \theta_2 + \frac{\widetilde{Q}_2}{\psi_{H_2}}\right] \frac{\gamma_{s,a}}{\tilde{\rho}_{s,a}(1-\phi_2)\xi_2 \xi_y \xi_z} \tag{7}$$

where $\gamma_{s,a} = c_{p,f}/c_{s,a}$, $c_{s,a}$ is the specific heat of the anode solid material, and $\tilde{\rho}_i$ is the dimensionless density defined by $\tilde{\rho}_i = \rho_i R_f T_\infty / p_\infty$.

In the anode reaction layer (CV3), the electrical current is generated by the electrochemical oxidation reaction,

$$H_{2(g)} \rightarrow 2H^+_{(aq)} + 2e^- \tag{8}$$

where a perfluorosulfonic acid membrane (e.g., Nafion 117 by DuPont) has been assumed in the electrolyte. CV3 is divided into two compartments, the solid and the ionomer that form the anode reaction layer. However, in the thermal analysis only the solid is taken into account, because the mass of ionomer in CV3 is negligible in comparison with the mass of solid. The dimensionless net heat transfer in CV3 is given by $\widetilde{Q}_3 = -\widetilde{Q}_{23} + \widetilde{Q}_{w3} + \widetilde{Q}_{34} + \widetilde{Q}_{3ohm}$. The heat transfer rate between CV3 and CV4 (the polymer electrolyte membrane) is dominated by conduction, therefore $\widetilde{Q}_{34} = -(1-\phi_3)(\theta_3-\theta_4)\widetilde{A}_s 2\widetilde{k}_{s,a}\widetilde{k}_p/(\xi_4\widetilde{k}_{s,a} + \xi_3\widetilde{k}_p)$.

The mass and energy balances for CV3, together with the anode reaction equation deliver the relations $\dot{n}_{H_2} = \dot{m}_{H_2}/M_{H_2}$, $\dot{n}_{H^+} = 2\dot{n}_{H_2}$, $\dot{m}_{H^+} = 2\dot{n}_{H_2} M_{H^+}$ and

$$\frac{d\theta_3}{d\tau} = \left[\widetilde{Q}_3 - \Delta\widetilde{H}_3 + \Delta\widetilde{G}_3\right] \frac{\gamma_{s,a}}{\tilde{\rho}_{s,a}(1-\phi_3)\xi_3 \xi_y \xi_z} \tag{9}$$

where $(\Delta\widetilde{H}_3, \Delta\widetilde{G}_3) = \dot{n}_{H_2}(\Delta H_3, \Delta G_3)/(\dot{m}_{ref} c_{p,f} T_\infty)$.

The dimensionless enthalpy of formation is defined by $\widetilde{H}_i = \dot{n}_i H_i/(\dot{m}_{ref} c_{p,f} T_\infty)$, where the subscript i refers to a substance or a control volume. The enthalpy change due to the anode reaction is given by $\Delta H_3 = \sum_{products}[\nu_i H_i(T_i)] - \sum_{reactants}[\nu_i H_i(T_i)]$ and $W_{e3} = -\Delta G_3$, ΔH_3 is the CV3 reaction enthalpy change (kJ/kmol H_2); ν_i are the stoichiometric coefficients; $H_i(T_i)$ is the molar enthalpy (kJ/kmol) of formation at a temperature T_i of reactants and products of compound i; ΔG_3 is the CV3 reaction Gibbs free energy change (kJ/kmol H_2) and W_{e3} is the maximum (reversible) electrical work generated due to the reaction in CV3 (kJ/kmol H_2).

The molar enthalpies of formation are obtained from tabulated values [32,33] at T_2 for $H_{2(g)}$ and T_3 for $H^+_{(aq)}$, and at 1 atm, because ΔH is independent of pressure. The reaction Gibbs free energy change ΔG is a function of temperature, pressure and concentrations,

$$\Delta G = \Delta G^\circ + \overline{R} T \ln Q \tag{10}$$

where $\Delta G^\circ = \Delta H^\circ - T\Delta S^\circ$ is the standard Gibbs free energy (kJ/kmol H_2); ΔH° is the standard enthalpy

change (kJ/kmol); ΔS° is the standard entropy change (kJ/kmol K^{-1}) [gases at 1 atm, 25 °C, species in solution at 1 M, where M is the molarity = (moles solute)/(liters solution)], and Q is the reaction quotient. The reaction quotient Q has the same mathematical form as the reaction equilibrium constant: the difference is that the terms that appear in Q are instantaneous pressures and concentrations rather than equilibrium values. Therefore, in the present reaction [Eq. (8)] the resulting expression for Q_3 is $Q_3 = [H^+_{(aq)}]^2/p_{H_2}$, where $[H^+_{(aq)}]$ is the molar concentration of the acid solution, (moles/l), and $p_{H_2} = p_{2,out}$, i.e., the partial pressure of H_2 in atmospheres at the CV2 outlet. Recall that pure liquids or solids do not appear in the calculation of Q_3; neither does the solvent in a dilute solution.

In a polymer electrolyte membrane, the water content (λ) is described as the ratio of the number of water molecules to the number of charge sites, i.e., the number of ions, $SO_3^- H^+$. Zawodzinski et al. [34] measured water content for the Nafion 117 membrane, and found that, for equilibrium with saturated water vapor, $\lambda = 14$ at 30 °C. Springer et al. [9] found that water vapor and liquid water (in equilibrium with each other) equilibrate separately to different membrane water contents, namely, $\lambda = 16.8$ at 80 °C and $\lambda = 22$ at 100 °C. Usually, the anode water content in the anode is different than in the cathode [28]; therefore for assumed values of λ_a (anode water content) and λ_c (cathode water content), and by assuming a linear variation of the water content along the membrane thickness, the average water content in the membrane is defined as

$$\lambda = \frac{\lambda_a + \lambda_c}{2} \tag{11}$$

Eq. (11) allows the calculation of $[H^+_{(aq)}]$ as a function of λ, namely $[H^+_{(aq)}] \cong \rho_{wa}/(\lambda M_{H_2O})$ for a dilute water solution. The present model also assumes that the volume fraction of ionomer in the catalyst layer is approximately equal to the porosity either in CV3 or CV5.

The reversible electrical potential at the anode is given by the Nernst equation [33],

$$V_{e,a} = V^{\circ}_{e,a} - \frac{\overline{R}T_3}{nF} \ln Q_3 \tag{12}$$

where $V_{e,a} = \Delta G_3/(-nF)$ and $V^{\circ}_{e,a} = \Delta G^{\circ}_3/(-nF)$. At the anode there are two mechanisms for potential losses: (i) charge transfer, and (ii) mass diffusion. The potential loss due to charge transfer is obtained implicitly from the Butler–Volmer equation for a given current I [35,36]

$$\frac{I}{A_{3,wet}} = i_{o,a}\left[e^{\frac{(1-\alpha_a)\eta_a F}{\overline{R}T_3}} - e^{-\frac{\alpha_a \eta_a F}{\overline{R}T_3}} \right] \tag{13}$$

where η_a is the potential loss at the anode, α_a is the anode charge transfer coefficient, and $i_{o,a}$ is the anode exchange current density (a function of catalyst type, catalyst layer morphology, temperature and pressure). The potential loss due to mass diffusion is [35]

$$\eta_{d,a} = \frac{\overline{R}T_3}{nF} \ln\left(1 - \frac{I}{A_{3,wet} i_{Lim,a}}\right) \tag{14}$$

In Eq. (14) the limiting current density at the anode ($i_{Lim,a}$) occurs at high values of the surface overpotential, when the gas is completely depleted in the very thin layer of active catalyst situated at the interface with the gas diffuser, i.e., $P_{2,out} = 0$. Therefore, Eq. (6) is rearranged to obtain $i_{Lim,a} = P_f p_\infty D_2 nF/(M_{H_2} L_2 R_f \theta_2 T_\infty)$.

The dimensionless potentials are defined based on a reference voltage, $\widetilde{V}_i = V_i/V_{ref}$ and $\tilde{\eta} = \eta_i/V_{ref}$, where subscript i accounts for all the potentials that are present in the fuel cell. The resulting electrical potential at the anode is $\widetilde{V}_{i,a} = \widetilde{V}_{e,a} - \tilde{\eta}_a - |\tilde{\eta}_{d,a}|$, where we have taken the absolute value of $\tilde{\eta}_{d,a}$, because $\tilde{\eta}_{d,a} < 0$ (cathodic overpotential).

Next is the analysis of the polymer electrolyte membrane (CV4), which interacts with CV3, CV5 and the ambient. In the cathode reaction layer (CV5), the reaction is

$$\frac{1}{2} O_{2(g)} + 2e^- + 2H^+_{(aq)} \rightarrow H_2O_{(l)} \tag{15}$$

Eqs. (8) and (15) and the conservation of mass in CV4 require $2\dot{n}_{H_2} = \dot{n}_{H^+_{out}} = \dot{n}_{H^+_{in}} = 2\dot{n}_{O_2}$. In conclusion, $\dot{n}_{O_2} = \dot{n}_{H_2}$, where $\dot{n}_{O_2} = 2\dot{m}_{O_2}/M_{O_2}$. Accordingly, the required oxidant mass flow rate is $\dot{m}_{O_2} = \dot{m}_{H_2} M_{O_2}/(2M_{H_2})$. The net heat transfer in CV4 is obtained from $\widetilde{Q}_4 = -\widetilde{Q}_{34} + \widetilde{Q}_{w4} + \widetilde{Q}_{45} + \widetilde{Q}_{4ohm}$ and $\widetilde{Q}_{45} = -(1-\phi_5)(\theta_4 - \theta_5)\widetilde{A}_s 2\widetilde{k}_{s,c}\widetilde{k}_{pm}/(\xi_4\widetilde{k}_{s,c} + \xi_5\widetilde{k}_{pm})$. Next, the CV4 temperature is obtained from

$$\frac{d\theta_4}{d\tau} = \left[\widetilde{Q}_4 + \widetilde{H}(\theta_3)_{H^+_{(aq)}} - \widetilde{H}(\theta_4)_{H^+_{(aq)}}\right] \frac{\gamma_{pm}}{\tilde{\rho}_{pm}\xi_4\xi_y\xi_z} \tag{16}$$

where $\gamma_{pm} = c_{p,f}/c_{pm}$, and c_{pm} is the polymer electrolyte membrane specific heat.

The internal ohmic losses are usually dominated by the low electrolyte conductivity. However in order to study of the effect of varying the thickness of the reacting layers, the model also accounts for the potential loss due to the electrical resistance posed by the ionomer within the porous reaction layers present in CV3 and CV5. The ionic conductivity, σ ($\Omega^{-1}\,m^{-1}$), of Nafion 117 as a function of temperature is given by the empirical formula [9]

$$\sigma_i(\theta) = \exp\left[1268\left(\frac{1}{303} - \frac{1}{\theta_i T_\infty}\right)\right](0.5139\lambda_i - 0.326), \quad i = 3,4,5 \tag{17}$$

Based on the electrical conductivities and geometry of each compartment, the electrical resistances, β (Ω) are given by $\beta_i = \xi_i/\widetilde{A}_s V_T^{1/3}\sigma_i(1-\phi_i)$, $i = 1,2,6,7$, and

$\beta_i = \xi_i/\widetilde{A}_s V_T^{1/3}\sigma_i\phi_i$, $i = 3,4,5$ ($\phi_4 = 1$). Therefore, the total dimensionless ohmic loss in the space from CV1 to CV7 is

$$\tilde{\eta}_{ohm} = \frac{I}{V_{ref}}\sum_{i=1}^{7}\beta_i \tag{18}$$

The conductivities of the catalyst layers are given by $\sigma_3\phi_3$ and $\sigma_5\phi_5$ [cf. Eq. (17)], and agree qualitatively with previously measured catalyst layers ionic conductivities [37], i.e., the ionic conductivity increases with increasing Nafion content, which increases as ϕ increases in the present model. Additionally, as a quantitative example, the product $\sigma\phi$ leads to a resistivity of 40.29 Ω cm, for $\lambda = 14$, $\phi = 0.2$ and $T = 80$ °C, which agrees with a previously reported catalyst layer electronic resistivity of 40 Ω cm [38]. The conductivities of the diffusive layers, σ_2 and σ_6, are the carbon-phase conductivities [12]. Finally, the conductivities of CV1 and CV7, σ_1 and σ_7, are the electrical conductivities of the bipolar plates material. The void fractions of CV1 and CV7 are accounted for, i.e., $\phi_1 = \phi_7 = \xi_c/(\xi_t + \xi_c)$, computed for any particular fuel cell internal geometry according to Fig. 2.

The analysis in the cathode reaction layer (CV5) is analogous to what we presented for the anode reaction layer (CV3). This time the reaction equation is Eq. (15). CV5 is also divided into two compartments, fluid and solid, but in the thermal analysis only the solid is taken into account. The dimensionless net heat transfer in CV5 is given by $\widetilde{Q}_5 = -\widetilde{Q}_{45} + \widetilde{Q}_{w5} + \widetilde{Q}_{56} + \widetilde{Q}_{5ohm}$, with $\widetilde{Q}_{56} = -\tilde{k}_{s,c}(1-\phi_6)\widetilde{A}_s(\theta_5 - \theta_6)/[(\xi_5 + \xi_6)/2]$.

The mass and energy balances in CV5, together with Eq. (15) deliver $\dot{n}_{H^+_{in}} = 2\dot{n}_{O_2}$, $\dot{n}_{H_2O,out} = \dot{n}_{O_2}$, and

$$\frac{d\theta_5}{d\tau} = \left[\widetilde{Q}_5 - \Delta\widetilde{H}_5 + \Delta\widetilde{G}_5\right]\frac{\gamma_{s,c}}{\tilde{\rho}_{s,c}(1-\phi_5)\xi_5\xi_y\xi_z} \tag{19}$$

where $(\Delta\widetilde{H}_5, \Delta\widetilde{G}_5) = \dot{n}_{O_2}(\Delta H_5, \Delta G_5)/(\dot{m}_{ref}c_{p,f}T_\infty)$. The enthalpy change during cathode reaction is $\Delta H_5 = \sum_{products}[\nu_i H_i(T_i)] - \sum_{reactants}[\nu_i H_i(T_i)]$, while $W_{e5} = -\Delta G_5$. Similarly to the anode analysis, the molar enthalpies of formation, $H_i(T_i)$, are obtained from tabulated values at T_6 for $O_{2(g)}$, T_4 for $H^+_{(aq)}$ and T_5 for $H_2O_{(l)}$ at 1 atm. The change in the Gibbs free energy ΔG_5 for the reaction of Eq. (15) is calculated by using Eq. (10). The CV5 reaction quotient is therefore $Q_5 = \{[H^+_{(aq)}]^2 p_{O_2}^{1/2}\}^{-1}$, where $p_{O_2} = p_{6,out}$. The reversible electrical potential at the cathode results from Eq. (12) after using $V_{e,c}$, $V^\circ_{e,c}$, ΔG_5, ΔG°_5, T_5 and Q_5 in place of $V_{e,a}$, $V^\circ_{e,a}$, ΔG_3, ΔG°_3, T_3 and Q_3.

The analysis for the cathode reaction layer (CV5) follows the same path as for the anode reaction layer (CV3). The potential losses are due to charge transfer and mass diffusion. The potential loss due to charge transfer is obtained through Eq. (13), using $A_{5,wet}$, $i_{o,c}$, α_c, η_c and T_5, in place of $A_{3,wet}$, $i_{o,a}$, α_a, η_a and T_3, respectively. The potential loss due to mass diffusion is calculated based on Eq. (14) by using $\eta_{d,c}$, T_5, $A_{5,wet}$ and $i_{Lim,c}$, in place of $\eta_{d,a}$, T_3, $A_{3,wet}$ and $i_{Lim,a}$, respectively. The limiting current density at the cathode ($i_{Lim,c}$), is calculated using the same reasoning as for CV3, based on Eq. (6), such that $i_{Lim,c} = 2P_{ox}p_\infty D_6 nF/(M_{O_2}L_6R_{ox}\theta_6T_\infty)$. Finally, the dimensionless electrical potential at the cathode is $\widetilde{V}_{i,c} = \widetilde{V}_{e,c} - \tilde{\eta}_c - |\tilde{\eta}_{d,c}|$.

The mass balance for CV6 yields $\dot{m}_{O_{2,out}} = \dot{m}_{O_{2,in}} = \dot{m}_{O_2}$ and $\dot{n}_{H_2O} = \dot{n}_{H_2O,out} = \dot{n}_{H_2O,in} = \dot{n}_{O_2}$. The dimensionless net heat transfer rate in CV6 results from $\widetilde{Q}_6 = -\widetilde{Q}_{56} + \dot{Q}_{w6} + \widetilde{Q}_{67} + \widetilde{Q}_{6ohm}$, with $\widetilde{Q}_{67} = \tilde{h}_7\widetilde{A}_s(1-\phi_6)(\theta_7 - \theta_6)$, $\tilde{h}_7 = h_7V_T^{2/3}/(\dot{m}_{ref}c_{p,f})$. The dimensionless temperature for CV6 is given by

$$\frac{d\theta_6}{d\tau} = \left[\widetilde{Q}_6 + \psi_{O_2}\frac{c_{p,ox}}{c_{p,f}}(\theta_7 - \theta_6) + \widetilde{H}(\theta_5)_{H_2O} - \widetilde{H}(\theta_6)_{H_2O}\right] \times \frac{\gamma_{s,c}}{\tilde{\rho}_{s,c}(1-\phi_6)\xi_6\xi_y\xi_z} \tag{20}$$

The dimensionless net heat transfer rate in CV7 is $\widetilde{Q}_7 = -\widetilde{Q}_{67} + \widetilde{Q}_{w7} + \widetilde{Q}_{7ohm}$. The balances for mass and energy in the oxidant channel (CV7), the assumptions of non-mixing incompressible flow, and the assumption that the space is filled mainly with dry oxygen, yield $\dot{m}_{H_2O} = \dot{m}_{H_2O,in} = \dot{m}_{H_2O,out} = \dot{n}_{O_2}M_{H_2O}$ and

$$\frac{d\theta_7}{d\tau} = \left[\widetilde{Q}_7 + \psi_{ox}\frac{c_{p,ox}}{c_{p,f}}(\theta_{ox} - \theta_7) + \widetilde{H}(\theta_6)_{H_2O} - \widetilde{H}(\theta_7)_{H_2O}\right] \times \frac{R_{ox}\theta_{7,0}\gamma_{ox}}{R_fP_{ox}n_c\xi_7\xi_c\xi_z} \tag{21}$$

where $\theta_{7,0}$ is a specified initial condition, and $\psi_{ox} = \zeta_7\psi_{O_2}$.

3. Constructal design

The model presented in Section 2 allows the calculation of the electrical power output of a single PEMFC when its geometry and operating parameters change. The model accounts for internal temperature and pressure gradients and potential losses. An important step in constructal design is the identification of realistic design constraints. As it was stated before Eq. (2), the total PEMFC stack volume, V_T, is fixed in the optimization process. In dimensionless terms, the volume constraint reads as $\xi_x\xi_y\xi_z = 1$. According to Fig. 1, in the PEMFC stack, the number of single cells is given by $n_s = \xi_x/\xi_s$, where $\xi_s = L_s/V_T^{1/3}$, and L_s is the total length (or thickness) of a single cell, as it is shown in Fig. 2.

Proceeding the analysis, it is necessary to account for the pressure drops in the gas channels of the single cells, and also in the input and output headers, as shown schematically in Fig. 3. The calculation of the total pressure drops in the fuel cell stack will lead to the required total

pumping power to supply the stack with fuel and oxidant at any current level.

The stoichiometric ratios in the fuel and oxidant channels, ζ_1 and ζ_7, are assumed known as specified operating parameters. Therefore, the inlet mass flow rates are $\psi_f = \zeta_1 \psi_{H_2}$ and $\psi_{ox} = \zeta_7 \psi_{O_2}$.

The pressure drops in the gas channels, from the input headers to the output headers, are given by the pressure drops in a single cell only, because they are in parallel (Fig. 3). The resulting dimensionless expression for rectangular shaped gas channels, accounting for the flow directional change (90° at the cell inlet and outlet), contraction (inlet) and expansion (outlet), together with the ideal gas model, is the following:

$$\Delta P_i = \left[f_i \left(\frac{\xi_z}{\xi_i} + \frac{\xi_z}{\xi_c} \right) + \frac{K_{bc}}{2} + \frac{K_{be}}{2} \right] \frac{P_j}{\theta_i} \frac{R_f}{R_j} \tilde{u}_i^2 \tag{22}$$

where $i = 1, 7$ and $j = f, ox$, respectively. Here $\tilde{u}_i = (\tilde{u}_{i,in} + \tilde{u}_{i,out})/2$ is the gas dimensionless mean velocity in the channel, defined as $\tilde{u} = u/(R_f T_\infty)^{1/2}$, f is the friction factor, K_{bc} and K_{be} are the bending-contraction and bending-expansion coefficients, respectively. According to mass conservation, the flow dimensionless mean velocities in the gas channels are $\tilde{u}_1 = C\theta_1(\psi_f - \psi_{H_2}/2)/(\widetilde{A}_{c1} P_f)$, $\tilde{u}_7 = R_{ox} C \theta_7 (\psi_{ox} - \psi_{O_2}/2)/(R_f \widetilde{A}_{c7} P_{ox})$, where $C = (R_f T_\infty)^{1/2} \dot{m}_{ref}/(p_\infty V_T^{2/3})$, and $\widetilde{A}_{ci} = n_c L_c L_i / V_T^{2/3}$, $i = 1, 7$, is the dimensionless total duct cross-section area in the fuel and oxidant channels, respectively.

The model also requires the evaluation of the friction factor and heat transfer coefficients in the gas channels. For the laminar regime ($Re_{D_h} < 2300$) we used the correlations [39]

$$f_i Re_{D_{h,i}} = 24(1 - 1.3553\delta_i + 1.9467\delta_i^2 - 1.7012\delta_i^3 + 0.9564\delta_i^4 - 0.2537\delta_i^5) \tag{23}$$

$$\frac{h_i D_{h,i}}{k_i} = 7.541(1 - 2.610\delta_i + 4.970\delta_i^2 - 5.119\delta_i^3 + 2.702\delta_i^4 - 0.548\delta_i^5) \tag{24}$$

where $\delta_i = L_c/L_i$, for $L_c \leqslant L_i$ and $\delta_i = L_i/L_c$, for $L_c > L_i$; $D_{h,i} = 2L_c L_i/(L_c + L_i)$, $Re_{D_{h,i}} = u_i D_{h,i} \rho_i / \mu_i$ and $i = 1, 7$. The correlations used for the turbulent regime were [40]

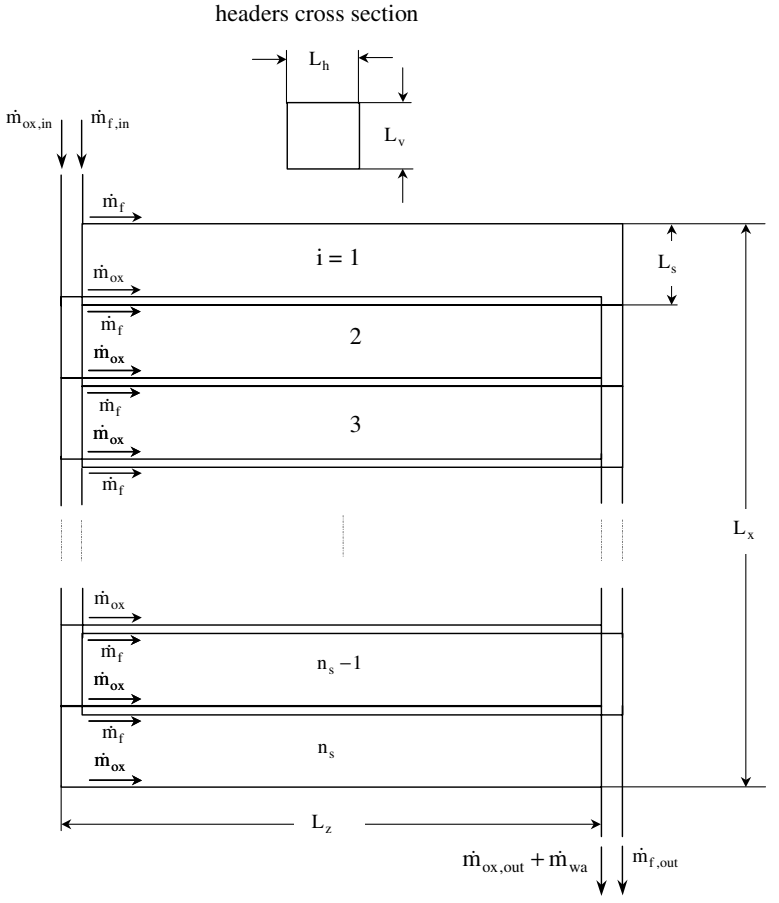

Fig. 3. Flow structure sketch of headers and gas channels in a PEMFC stack.

$$f_i = 0.079 Re_{D_{\mathrm{h}}}^{-1/4} \quad (2300 < Re_{D_{\mathrm{h},i}} < 2\times 10^4)$$
$$f_i = 0.046 Re_{D_{\mathrm{h}}}^{-1/5} \quad (2\times 10^4 < Re_{D_{\mathrm{h},i}} < 10^6) \tag{25}$$

$$\frac{h_i D_{\mathrm{h},i}}{k_i} = \frac{(f_i/2)(Re_{D_{\mathrm{h},i}} - 10^3)Pr_i}{1 + 12.7(f_i/2)^{1/2}(Pr^{2/3} - 1)} \quad (2300 < Re_{D_{\mathrm{h},i}} < 5\times 10^6) \tag{26}$$

where Pr is the gas Prandtl number, $\mu c_p/k$. Next, the pressure drops in the input and output headers are calculated according to the schematic diagram presented in Fig. 3. In the input headers, the inlet fuel and oxidant mass flow rates, $\psi_{\mathrm{f,in}} = n_{\mathrm{s}}\psi_{\mathrm{f}}$ and $\psi_{\mathrm{ox,in}} = n_{\mathrm{s}}\psi_{\mathrm{ox}}$, supply each single cell level with fuel and oxidant mass flow rates, ψ_{f} and ψ_{ox}, respectively. In the output headers, each single cell delivers depleted fuel and oxidant mass flow rates, and the water mass flow rate produced by the electrochemical reaction, $(\zeta_1 - 1)\psi_{\mathrm{f}}$, $(\zeta_7 - 1)\psi_{\mathrm{ox}}$, and $\psi_{\mathrm{H_2O}}$, respectively. Therefore, the fuel, oxidant and water mass flow rates in the headers vary according to each single cell level, and so do the flow mean velocities. As a result, the fuel and oxidant pressure drops in each segment of the headers adjacent to a single cell level "i", and the water flow pressure drop in the oxidant output header are calculated by

$$\Delta P_{i,k} = f_{i,k}\left(\frac{\xi_{\mathrm{s}}}{\xi_v} + \frac{\xi_{\mathrm{s}}}{\xi_{\mathrm{h}}}\right)\frac{P_j}{\theta_{i,k}}\frac{R_{\mathrm{f}}}{R_j}\tilde{u}_{i,k}^2$$
$$\Delta P_{\mathrm{wa},i} = f_i\left(\frac{\xi_{\mathrm{s}}}{\xi_v} + \frac{\xi_{\mathrm{s}}}{\xi_{\mathrm{h}}}\right)\tilde{\rho}_{\mathrm{wa}}\tilde{u}_{\mathrm{wa},i}^2 \tag{27}$$

where $k = h_{\mathrm{f,in}}, h_{\mathrm{ox,in}}, h_{\mathrm{f,out}}, h_{\mathrm{ox,out}}$ stand for input fuel (f) and oxidant (ox) headers, output fuel and oxidant headers, respectively. For Eq. (27), in the input headers the temperatures are the known inlet fuel and oxidant temperatures, and in the output headers, the temperatures are the temperatures of the fuel and oxidant exiting the single cell, calculated by the model, i.e., θ_1 and θ_7, respectively. Here $\tilde{u}$ is the dimensionless mean velocity, f is the friction factor calculated by Eq. (23), with $\delta_i = L_{\mathrm{h}}/L_{\mathrm{v}}$, for $L_{\mathrm{h}} \leqslant L_{\mathrm{v}}$ and $\delta_i = L_{\mathrm{v}}/L_{\mathrm{h}}$, for $L_{\mathrm{h}} > L_{\mathrm{v}}$; $D_{\mathrm{h},i} = 2L_{\mathrm{h}}L_{\mathrm{v}}/(L_{\mathrm{h}} + L_{\mathrm{v}})$, or by Eq. (25), for the laminar or turbulent flow regimes, respectively. According to mass conservation, the dimensionless gas mean velocities in the headers at each single cell level "i" in the stack are given by $\tilde{u}_{i,k} = C[R\theta\psi/(\phi P)]_{i,k}/(R_{\mathrm{f}}\widetilde{A}_{\mathrm{ch}})$, and for the water in the oxidant output header, $\tilde{u}_{\mathrm{wa},i} = C\psi_{\mathrm{wa},i}[\tilde{\rho}_{\mathrm{wa}}(1 - \phi_{i,h_{\mathrm{ox,out}}})\widetilde{A}_{\mathrm{ch}}]$, where $k = h_{\mathrm{f,in}}, h_{\mathrm{ox,in}}, h_{\mathrm{f,out}}, h_{\mathrm{ox,out}}$ represent the input fuel and oxidant headers, output fuel and oxidant headers; $\widetilde{A}_{\mathrm{ch}} = L_{\mathrm{h}}L_{\mathrm{v}}/V_{\mathrm{T}}^{2/3}$, is the dimensionless cross-section area in the fuel and oxidant headers; $\phi_{i,k} = 1$ for all headers, except in the oxidant output header, when $\phi_{i,k} < 1$ since oxidant and water flow in the header.

Finally, the gases dimensionless mass flow rates at each single cell level "i" are $\psi_{i,k} = \psi_{i-1,k} - \psi_j$, for $i = 1$ to n_{s}, and $j = \mathrm{H_2}$ or $\mathrm{O_2}$, with $\psi_{0,k} = \psi_{\mathrm{f,in}}$ or $\psi_{\mathrm{ox,in}}$, for the input headers, and for the output headers, $\psi_{i,k} = \psi_{i-1,k} + (\zeta_{\mathrm{g}} - 1)\psi_j$, for $i = 1$ to n_{s}, $g = 1$ or 7, and $j = \mathrm{f}$, ox, accordingly, with $\psi_{0,k} = 0$. The water mass flow rate at each single cell level "i" in the output oxidant header is $\psi_{\mathrm{wa},i} = \psi_{\mathrm{wa},i-1} + \psi_{\mathrm{H_2O}}$, for $i = 1$ to n_{s}, with $\psi_{\mathrm{wa},0} = 0$. Eqs. (22)–(27) deliver the pressure drops from the input to the output headers, ΔP_1 and ΔP_7, and the pressure drops in the input and output headers at each cell level, $\Delta P_{i,k}$ and $\Delta P_{\mathrm{wa},i}$, for each tested geometry during the constructal process.

According to Fig. 2, the architecture of the single fuel cell is determined completely by the internal structure ($L_{\mathrm{s}} = 2L_{\mathrm{b}} + \sum_{i=1}^{7} L_i$). The fuel cell stack external shape is given by (L_x, L_y, L_z) for a constrained total volume, V_{T}. The optimization objective is to determine the entire system architecture: the optimal volume allocation, such that the PEMFC stack total net power is maximized. The determination of the total stack net power starts with the single PEMFC polarization curve, i.e., the fuel cell total potential as a function of current, and the total net power (available for utilization) of a single fuel cell in the stack are given by

$$\widetilde{V}_i = \widetilde{V}_{i,\mathrm{a}} + \widetilde{V}_{i,\mathrm{c}} - \tilde{\eta}_{\mathrm{ohm}}, \quad \widetilde{W}_{\mathrm{net,s}} = \widetilde{W}_{\mathrm{s}} - \widetilde{W}_{\mathrm{p}} \tag{28}$$

where $\widetilde{W}_{\mathrm{s}} = \widetilde{V}_i\widetilde{I}$, and $\widetilde{W}_{\mathrm{p}} = \psi_{\mathrm{f}}S_{\mathrm{f}}\theta_1\Delta P_1/P_1 + \psi_{\mathrm{ox}}S_{\mathrm{ox}}\theta_7\Delta P_7/P_7$, with $S_j = \dot{m}_{\mathrm{ref}}T_\infty R_j/(V_{\mathrm{ref}}I_{\mathrm{ref}})$, $j = \mathrm{f}, \mathrm{ox}$.

Additional power is required to pump fuel, oxidant, and produced water in and out the headers shown in Fig. 3. The dimensionless pumping power required for the gases at the fuel cell level i, and for the produced water out of the oxidant output header are given by

$$\widetilde{W}_{i,k} = S_j\left[\frac{\psi\theta\Delta P}{P}\right]_{i,k}, \quad j = \mathrm{f}, \mathrm{ox},$$
$$\widetilde{W}_{\mathrm{wa},i} = \frac{S_{\mathrm{f}}}{\tilde{\rho}_{\mathrm{wa}}}[\psi\Delta P]_{\mathrm{wa},i} \tag{29}$$

The total PEMFC stack power available for utilization is therefore obtained from

$$\widetilde{W}_{\mathrm{net}} = n_{\mathrm{s}}(\widetilde{W}_{\mathrm{s}} - \widetilde{W}_{\mathrm{p}}) - \sum_{k}\sum_{i=1}^{n_{\mathrm{s}}}\widetilde{W}_{i,k} - \sum_{i=1}^{n_{\mathrm{s}}}\widetilde{W}_{\mathrm{wa},i} \tag{30}$$

where $k = h_{\mathrm{f,in}}, h_{\mathrm{ox,in}}, h_{\mathrm{f,out}}, h_{\mathrm{ox,out}}$. The objective function defined by Eq. (30) depends on the internal structure and thickness of each single cell, and on the external shape of the PEMFC stack. The mathematical model allows the computation of the total net power of the PEMFC stack, $\widetilde{W}_{\mathrm{net}}$. This is possible to achieve as soon as the physical values (Table 1) and a set of geometric internal ($1 = 2\xi_{\mathrm{b}}/\xi_{\mathrm{s}} + \sum_{i=1}^{7}\xi_i/\xi_{\mathrm{s}}$ and ξ_{s}) and external (ξ_y/ξ_x and ξ_z/ξ_x) parameters are chosen for the overall system. The maximum (theoretical) PEMFC stack efficiency is given by

Table 1
Physical properties used as reference case in the numerical optimization of the PEMFC stack

$B = 0.156$ [43]	$t_{ref} = 10^{-3}$ s
$c_{p,f} = 14.95$ kJ kg^{-1} K^{-1}	T_f, T_{ox}, $T_\infty = 298.15$ K
$c_{pm} = 4.18$ kJ kg^{-1} K^{-1}	$T_{Lim} = 373.15$ K
$c_{p,ox} = 0.91875$ kJ kg^{-1} K^{-1}	$U_{wi} = 50$ W m^{-2} K^{-1}, $i = 1,7$
$c_{v,f} = 10.8$ kJ kg^{-1} K^{-1}	$V_{ref} = 1$ V
$c_{v,ox} = 0.659375$ kJ kg^{-1} K^{-1}	$V_{T,ref} = 10^{-5}$ m^3
$i_{0,a}$, $i_{0,c} = 10$ A m^{-2}	α_a, $\alpha_c = 0.5$
$I_{ref} = 1$ A	$\mu_1 = 10^{-5}$ Pa s
$k_f = 0.2$ W m^{-1} K^{-1}	$\mu_7 = 2.4 \times 10^{-5}$ Pa s
$k_{ox} = 0.033$ W m^{-1} K^{-1}	$\xi_c/\xi_y = 0.005$
$k_{pm} = 0.21$ W m^{-1} K^{-1}	$\xi_h = \xi_v = 0.022$
$k_{s,a}$, $k_{s,c} = 71.6$ W m^{-1} K^{-1}	$\xi_t/\xi_y = 0.05$
K_{bc}, $K_{be} = 0.9$	$\rho_{wa} = 1000$ kg m^{-3}
K_2, $K_6 = 4 \times 10^{-14}$ m^2	σ_1, $\sigma_7 = 1.388 \times 10^6$ Ω^{-1} m^{-1}
K_3, $K_5 = 4 \times 10^{-16}$ m^2	σ_2, $\sigma_6 = 4000$ Ω^{-1} m^{-1}
p_r, $p_\infty = 0.1$ MPa	$\phi_{h_{ox,out}} = 0.5$
$p_{ox} = 0.12$ MPa	ϕ_2, $\phi_6 = 0.4$
$q = 1.5$	ϕ_3, $\phi_5 = 0.2$
$R_f = 4.157$ kJ kg^{-1} K^{-1}	
$R_{ox} = 0.2598$ kJ kg^{-1} K^{-1}	

$$\eta_i = \frac{\Delta\widetilde{G}_3 + \Delta\widetilde{G}_5}{\Delta\widetilde{H}_3 + \Delta\widetilde{H}_5} \tag{31}$$

The actual first-law efficiency of the fuel cell stack is

$$\eta_I = E\frac{\widetilde{W}_s}{\Delta\widetilde{H}_3 + \Delta\widetilde{H}_5} \tag{32}$$

where $E = V_{ref} I_{ref}/(\dot{m}_{ref} c_{p,f} T_\infty)$. The second-law efficiency is defined as the ratio of the actual electrical power to the reversible electrical power,

$$\eta_{II} = E\frac{\widetilde{W}_s}{\Delta\widetilde{G}_3 + \Delta\widetilde{G}_5} \tag{33}$$

The net efficiency of the PEMFC stack is

$$\eta_{net} = E\frac{\widetilde{W}_{net}}{n_s(\Delta\widetilde{H}_3 + \Delta\widetilde{H}_5)} \tag{34}$$

In previous studies [27,28] we found the optimal distribution of the compartments shown in Fig. 2 for fuel cell maximum power under a volume constraint, for an alkaline fuel cell, and for a single PEMFC where the external shape of the cell was allowed to vary. In this study, the constructal procedure seeks the PEMFC stack optimal internal structure, length (or thickness) of the single fuel cell, and external shape (ξ_y/ξ_x and ξ_z/ξ_x) based on the general configuration presented in Fig. 1, and according to the following algorithm:

1. Fix total PEMFC stack volume, $\widetilde{V}_T$, and assume a fuel cell square section, i.e., $\frac{\xi_y}{\xi_x} = \frac{\xi_z}{\xi_x}$.
2. Select the lowest value for $\frac{\xi_y}{\xi_x} = \frac{\xi_z}{\xi_x}$ within a pre-specified range of variation.
3. Compute ξ_x, ξ_y, ξ_z.
4. For $\widetilde{A}_s = \xi_y\xi_z$, vary the thickness of a single fuel cell, ξ_s within a pre-specified range.
5. For each ξ_s, find the optimal internal structure that delivers a maximum value for $\widetilde{W}_{net}$.
6. The result of the process of step 5 is $\xi_{s,opt}$ for $\widetilde{W}_{net,m}$, which is the maximum value of $\widetilde{W}_{net}$ found for all tested ξ_s in step 5.
7. Compute the resulting number of single cells in the stack: $n_{s,opt} = \frac{\xi_x}{\xi_{s,opt}}$, increment $\frac{\xi_y}{\xi_x} = \frac{\xi_z}{\xi_x}$ and return to step 2 until the entire $\frac{\xi_y}{\xi_x} = \frac{\xi_z}{\xi_x}$ pre-specified range is covered.
8. The result of the outer loop (2–7) is the optimized configuration of the PEMFC stack for maximum net power density that is possible to be obtained in a constrained total volume, V_T, given by Eq. (30):

$$\left(\frac{\xi_y}{\xi_x} = \frac{\xi_z}{\xi_x}, \begin{Bmatrix} n_s \\ \xi_s \end{Bmatrix}\right)_{opt} \Rightarrow \widetilde{W}_{net,mm}$$

The optimization of internal structure mentioned in step 5 of the optimization algorithm is executed following the procedure introduced by Vargas et al. [28] for a single PEMFC. First, the anode and cathode are assumed to have the same thickness. The thicknesses of the diffusion and reaction layers of the cathode and anode are varied simultaneously subject to fixed ratios of cathode thickness (y_2) and anode thickness (y_6) to total single cell length, i.e., $\xi_2/\xi_s + \xi_3/\xi_s = y_2$, $\xi_5/\xi_s + \xi_6/\xi_s = y_6$, where y_4 is the ratio of membrane thickness to total single cell length. The ratio of overall thickness to total length of the single fuel cell is also fixed, $y_2 + y_4 + y_6 = 0.8$. Under the simplifying hypotheses assumed, the internal structure optimization problem is reduced to one degree of freedom, i.e., the ratio $\xi_3/\xi_s = \xi_5/\xi_s$. The end result is the optimized configuration of the single fuel cell electrodes $(\xi_2, \xi_3, \xi_5, \xi_6)_{opt}$, for which the PEMFC stack net power, given by Eq. (30) is maximum.

The physical properties assumed in this study were suggested by previous studies and obtained from handbooks [9,11,12,35,41], and are listed in Table 1. Eqs. (4), (6), (7), (9), (16), (19)–(21), and the specified initial conditions form a system of seven ordinary differential equations and two algebraic equations. The unknowns are θ_i and P_i, i.e., the temperatures in the seven control volumes, and the gas pressures in CV2 and CV6. Once the temperatures and pressures are known, the electrical potentials, electrical power, and PEMFC stack net power can be calculated for any current level.

Two numerical methods are used. The first method calculates the transient behavior of the system, starting from a set of initial conditions, then the solution is marched in time (and checked for accuracy) until a steady state is achieved at any current level. The equations are integrated in time explicitly using an adaptive time step, fourth to fifth order Runge–Kutta method [42]. The time step is adjusted automatically according to

the local truncation error, which is kept below a specified tolerance of 10^{-6}. The second method is for the steady state solution. The time derivatives are dropped from Eqs. (4), (7), (9), (16), (19)–(21). Pressures are related to temperatures via Eq. (6). The system reduces to seven nonlinear algebraic equations, in which the unknowns are the temperatures of the seven control volumes. This system is solved using a quasi-Newton method [42]. Convergence was achieved when the Euclidean norm of the residual of the system was less than 10^{-6}.

4. Results and discussion

In the procedure described by the algorithm presented in Section 3, the PEMFC stack net power is calculated by starting from open circuit ($\widetilde{I}=0$) and proceeding in pre-specified increments $\Delta\widetilde{I}$ (e.g., 2, 5, 10) until the net power is zero, the membrane limiting operating temperature is achieved, T_{Lim}, or the limiting current level is reached. This procedure is illustrated in Fig. 4, which shows simulation results for one selected PEMFC stack external shape ($\xi_y/\xi_x=\xi_z/\xi_x=0.3$), which has been optimized according to step 5 of the algorithm of Section 3, i.e., an optimal internal structure and single cell thickness ($\xi_s=0.0044$) was found for that particular external shape. The resulting electrical power, and polarization curves of a single cell, and the PEMFC stack net power curves are shown in Fig. 4a. According to the model, the actual open circuit voltage is equal to the reversible cell potential, because it has been assumed that no losses result from species crossover from one electrode through the electrolyte, and from internal currents. The change in the Gibbs free energy of reaction decreases as the temperature increases. Therefore, according to Eq. (12) the reversible electrical potential decreases as the temperature increases, which happens when the current increases.

In Fig. 4a, the simulation stopped when the temperature at any compartment of the single fuel cell reached the limiting membrane operating temperature, i.e., $\theta_i \leqslant \theta_{\mathrm{Lim}}$, and at this point $\widetilde{W}_{\mathrm{net}}>0$ for the selected configuration under analysis. The other ending criterion is $\widetilde{W}_{\mathrm{net}}=0$, i.e., up to the point where the electrical power produced by the PEMFC stack matched the required pumping power to supply fuel and oxidant to the stack at any specified stoichiometric ratios $\zeta_1=\zeta_7$. Under such selected operating conditions and geometry ($\xi_y/\xi_x=\xi_z/\xi_x=0.3$), the PEMFC stack did not reach the concentration polarization region as $\widetilde{V}_{\mathrm{e,a}}$ or $\widetilde{V}_{\mathrm{e,c}}$ would approach zero. The net power curve exhibits a maximum at $\widetilde{I}\approx 250$, which is central in the evaluation of global performance, by balancing total electrical power produced with required pumping power to supply fuel and oxidant to the PEMFC stack. The maximum net power is the quantity maximized during the constructal

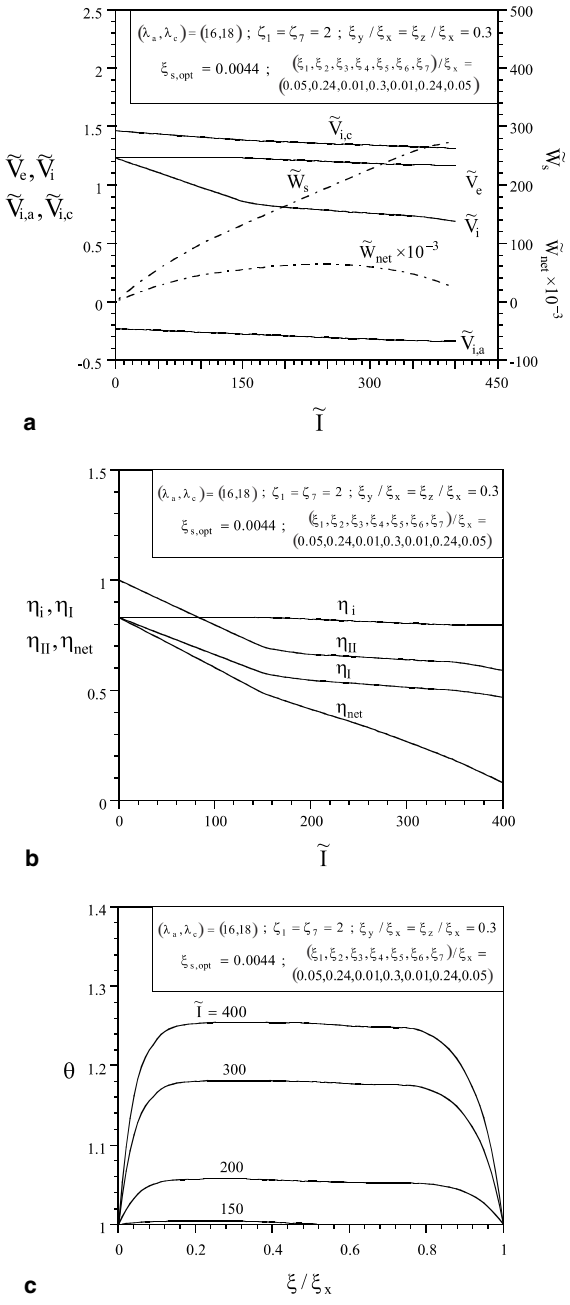

Fig. 4. (a) Example of single PEMFC polarization, total electrical power and PEMFC stack net power output curves; (b) the ideal, first law, second law and net efficiencies for the PEMFC stack considered in (a), and (c) the behavior of temperature versus flow length for several current levels, in a single PEMFC for the stack considered in (a) and (b).

procedure described by the algorithm presented in Section 3.

Fig. 4b shows that the ideal efficiency (η_i) decreases as the current increases. This effect is due to the

temperature increase in the anode and cathode reaction layers, which is captured by the present model. The first law efficiency is equal to the ideal efficiency at open circuit ($\widetilde{I} = 0$), and decreases monotonically as the current increases. The second law efficiency is equal to 1 (reversible operation, no losses) at open circuit ($\widetilde{I} = 0$), and also decreases monotonically as the current increases. The net efficiency behavior shows the effect of increasing current and therefore pressure drops in the single cells gas channels and fuel and oxidant input and output headers, i.e., the pumping power increases and the net power decreases, eventually reaching a zero limit when $\widetilde{W}_{\text{net}} = 0$.

The fuel flow rate increases as the current increases, Eq. (1), therefore more heat is generated by the reactions at the anode and cathode, increasing the temperature. The temperatures in the single fuel cell compartments shown in Fig. 2 increase as the current increases, as shown in Fig. 4c, because more heat is generated by the electrochemical reaction and by Joule effect (ohmic heating). The higher the current, the more accentuated are the temperature spatial gradients between the single fuel cell compartments, even for the single fuel cell considered in Fig. 4, with the selected high geometric aspect ratio ξ_y, $\xi_z \gg \xi_{s,opt}$ ($\xi_y/\xi_s = \xi_z/\xi_s = 152$), i.e., with a small thickness compared to width and height. Therefore, the PEMFC stack net power and polarization curves produced by the present model take into account all the internal spatial temperature gradients, which affect the polarization curve and the total electrical power output. Most importantly, the spatial temperature distribution results of Fig. 4c show that, although a cooling system is considered across the bipolar plates with an externally controlled and monitored average temperature T_∞, the actual single cell internal temperature is substantially higher than that. This finding should be considered in fuel cell design.

Fig. 5 shows the start-up transient—the evolution of the temperatures and net power until steady state is reached at a high current level ($\widetilde{I} = 250$) required by the load. In Fig. 5a, there is a considerable temperature spatial gradient between the internal compartments of the single fuel cell, and it affects fuel cell performance. Hydrogen is about ten times more thermally conductive than oxygen, therefore the fuel gas channel temperature is higher than the oxidant gas channel temperature, i.e., with a better thermal contact with the other internal compartments. The effect on PEMFC stack net power is documented in Fig. 5b. The net power increases monotonically as the internal cell temperatures increase, eventually reaching a plateau at steady state operation. A transient model is therefore mandatory if one is to evaluate fuel cell performance for simulations of applications with variable load.

Fig. 6 illustrates the constructal procedure for one set of external parameters, i.e., Table 1, $\zeta_1 = \zeta_7 = 2$,

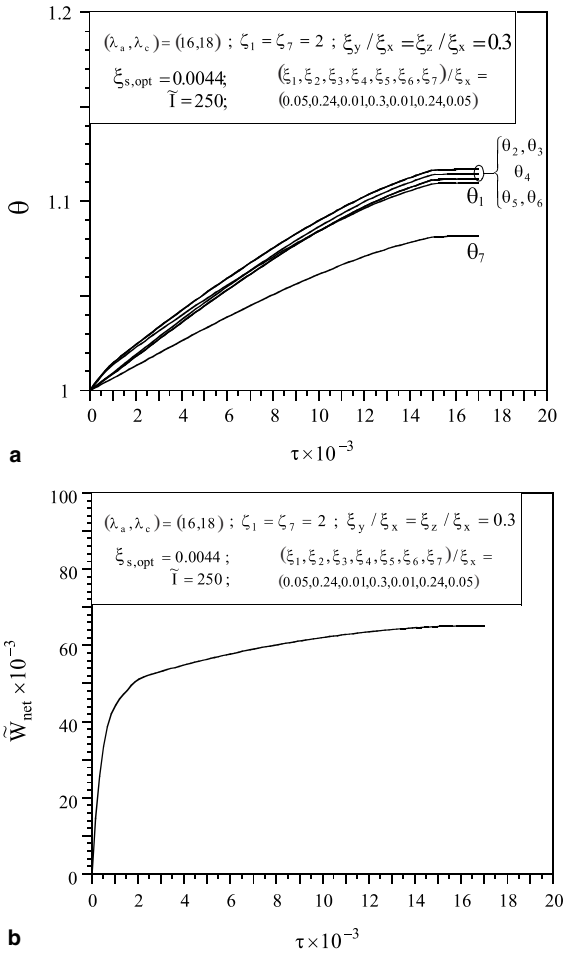

Fig. 5. (a) The transient response of the internal compartments temperatures in a single PEMFC for the stack considered in Fig. 4 and (b) the transient response of the PEMFC stack net power for the stack considered in Fig. 4.

$(\lambda_a, \lambda_c) = (16, 18)$, and $\widetilde{V}_T = 1.16$. The graphical results follow the steps of the algorithm presented in Section 3. Fig. 6a shows the results of steps 4, 5 and 6, which identify $\xi_{s,opt}$ for several PEMFC stack external shapes, $\xi_y/\xi_x = \xi_z/\xi_x$. For each value of ξ_s, a corresponding fuel cell optimal internal structure is found, but this is not shown in Fig. 6 for the sake of brevity. However, the bulk of results of this study for the optimized internal structure corroborate the results discussed and documented in the constructal optimization of a single PEMFC [28], i.e., $\xi_3/\xi_s = \xi_5/\xi_s \cong 0.01$. The optimal single cell thickness $\xi_{s,opt}$ results from the trade-off between two effects: activation polarization losses and ohmic losses. As ξ_s increases, the electrode wetted areas increase, thus the activation losses decrease. On the other hand, the ohmic losses increase as thickness increases. Another interesting phenomenon is that the

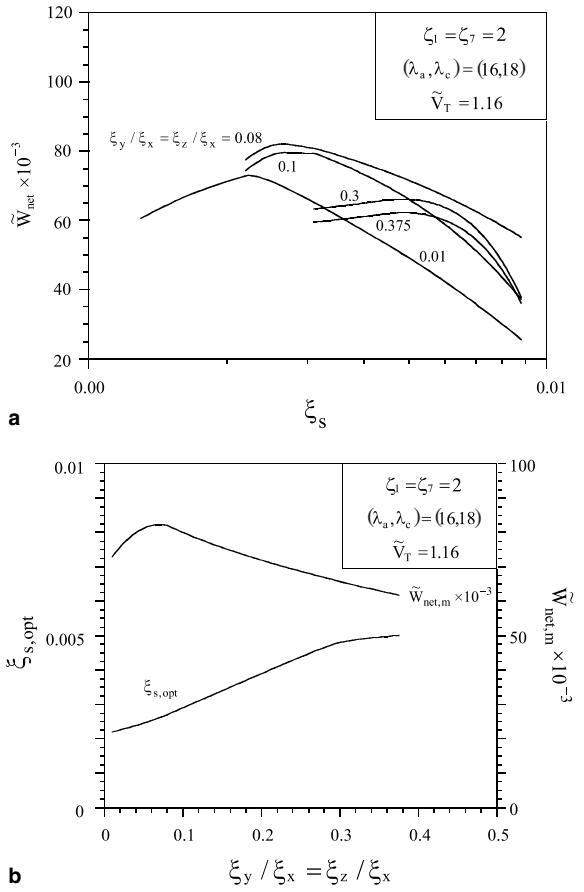

Fig. 6. (a) The internal structure and single cell thickness optimization according to Fig. 2 and the dependence on external shape of the PEMFC stack, and (b) the existence of a maximum PEMFC stack net power and the corresponding optimized single cell thickness with respect to external shape of the stack.

ionomer electrical conductivity increases as temperature increases at higher current levels, and with water content increase as well, therefore reducing ohmic loss at higher temperatures, which is represented by Eq. (17). The results of those trade-offs observed during single cell thickness variation in the optimization process is shown in Fig. 6a, which shows net power maxima for five PEMFC stack external geometric aspect ratios. Note that the single cell thickness is optimized for the maximum PEMFC stack net power, i.e., the optimization of the component shape for maximum performance of the global system. The maxima are sharp, stressing the importance of these optima found in future fuel cell design.

The results of Fig. 6a are summarized in Fig. 6b, which also shows the existence of a second maximum for the PEMFC stack net power, this time with respect to external geometric aspect ratios. The curves document the final steps of the optimization algorithm presented in Section 3, pinpointing the optimal single cell thickness and stack external shape for maximum net power output. The maximum is sharp, therefore important in fuel cell design. The existence of a PEMFC stack net power maximum with respect to stack external shape is explained by analyzing two extremes: (i) small $\xi_y/\xi_x = \xi_z/\xi_x$ implies that ξ_x is large, $\widetilde{W}_s$ is small due to large flow resistances in the x-direction, the number of single cells n_s is high, therefore the resulting total stack electrical power is still high, but the headers pumping power increase as ξ_x increases, therefore $\widetilde{W}_{net,m} \to 0$, and (ii) large $\xi_y/\xi_x = \xi_z/\xi_x$ implies that ξ_x is small, $\widetilde{W}_s$ is large due to small flow resistances in the x-direction and also large wetted areas at the electrodes, the headers pumping power decrease as ξ_x decreases, but $\widetilde{W}_p$ is also large due to a large swept length ξ_z and small hydraulic

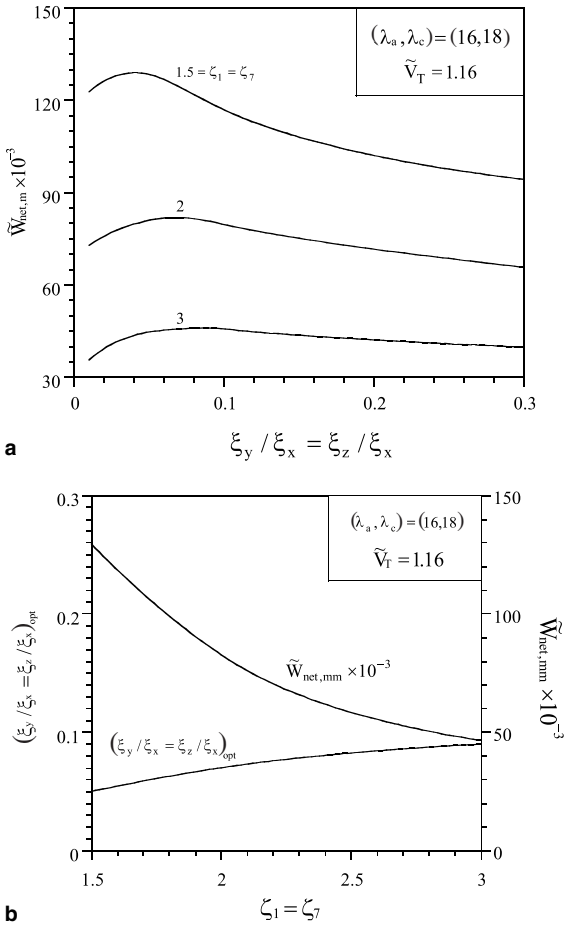

Fig. 7. (a) The external shape optimization and the dependence on stoichiometric ratio for $(\lambda_a, \lambda_c) = (16,18)$ and $\widetilde{V}_T = 1.16$, and (b) the results of the external shape optimization with respect to the stoichiometric ratios, $\zeta_1 = \zeta_7$, for $(\lambda_a, \lambda_c) = (16,18)$ and $\widetilde{V}_T = 1.16$.

diameters D_h, therefore $\widetilde{W}_{net,m} \to 0$ in this extreme as well. In conclusion, there must exist an intermediate and optimal $\xi_y/\xi_x = \xi_z/\xi_x$ geometric configuration such that $\widetilde{W}_{net,m}$ is maximum, which balances the trade-off between electrical power output and pumping power to supply fuel and oxidant to the PEMFC stack, according to Eq. (30).

In a subsequent phase of the study, a sensitivity analysis was conducted to find the dependence of the optimization results on the variation of three operating and design parameters, i.e., $\zeta_1 = \zeta_7$, (λ_a, λ_c), and $\widetilde{V}_T$. The PEMFC stack net power is plotted in Fig. 7a as a function of $\xi_y/\xi_x = \xi_z/\xi_x$ for three different stoichiometric ratios regimes, $\zeta_1 = \zeta_7$. For all stoichiometric ratios, a twice maximized stack net power, $\widetilde{W}_{net,mm}$, is observed, determining the optimal external PEMFC stack structure, represented by $(\xi_y/\xi_x = \xi_z/\xi_x)_{opt}$. As the stoichiometric ratios increase, the net power decreases because the fuel and oxidant mass flow rates in the headers and gas channels increase, and therefore pressure drops and pumping power increase. The maxima are sharp, mainly for lower stoichiometric ratios. Fig. 7b shows the twice maximized stack net power and the corresponding optimal external shapes as functions of the stoichiometric ratios. The stack net power $\widetilde{W}_{net,mm}$ decreases monotonically as the stoichiometric ratios increase. The reason for that is that as the stoichiometric ratios increase the pumping power increases as well. Most important is the observation that the optimal external geometry is robust with respect to changes in the stoichiometric ratios, i.e., for $1.5 \leqslant \zeta_1 = \zeta_7 \leqslant 3$, the optimal external shape varied only slightly, i.e., $0.05 \leqslant (\xi_y/\xi_x = \xi_z/\xi_x)_{opt} \leqslant 0.08$.

Next, the effect of the variation of membrane water content, $\lambda = (\lambda_a + \lambda_c)/2$, based on specified pairs (λ_a, λ_c) was investigated. The results of Fig. 8a show stack net power maxima for three different combinations of (λ_a, λ_c). As the water content increases, the twice maximized net power also increases, which is explained by

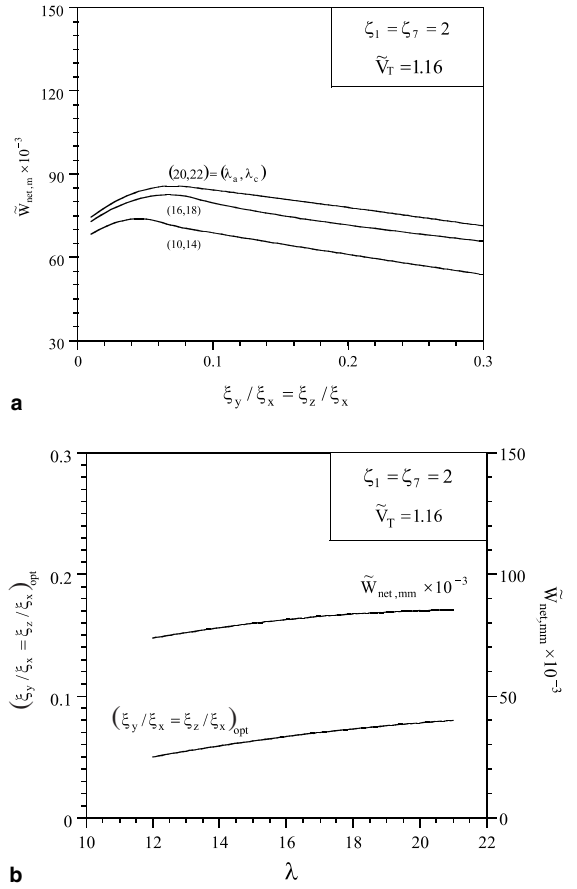

Fig. 8. (a) The external shape optimization and the dependence on average membrane water content for $\zeta_1 = \zeta_7 = 2$ and $\widetilde{V}_T = 1.16$, and (b) the results of the external shape optimization with respect to average membrane water content, λ, $\zeta_1 = \zeta_7 = 2$ and $\widetilde{V}_T = 1.16$.

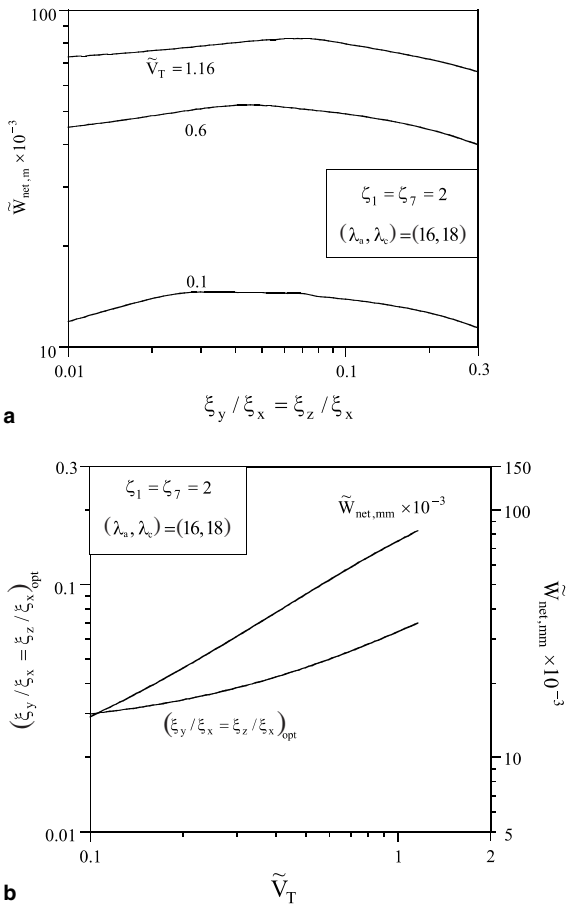

Fig. 9. (a) The external shape optimization and the dependence on total stack volume for $(\lambda_a, \lambda_c) = (16, 18)$ and $\zeta_1 = \zeta_7 = 2$, and (b) the results of the external shape optimization with respect to total stack volume, $\widetilde{V}_T$, for $(\lambda_a, \lambda_c) = (16, 18)$ and $\zeta_1 = \zeta_7 = 2$.

higher membrane electrical conductivities and smaller ohmic losses. Fig. 8b summarizes the optimization results showing the twice maximized net power and the corresponding optimized stack external shapes. The optimized external shape is also robust with respect to the variation of membrane water content.

The investigation of the variation of the volume constraint is conducted in Fig. 9, where $\widetilde{V}_T$ was varied over the range 0.1–1.16, for stoichiometric ratios $\zeta_1 = \zeta_7 = 2$. This variation is indicated by the three curves of Fig. 9a. All curves exhibit PEMFC stack maxima with respect to the external shape aspect ratios. The fuel cell stack net power increases as $\widetilde{V}_T$ increases. Additional results were produced to cover the entire range $0.1 \leqslant \widetilde{V}_T \leqslant 1.16$, which allowed the twice maximized stack net power and the optimized external shape aspect ratios to be plotted in Fig. 9b as functions of $\widetilde{V}_T$. The twice maximized stack net power increases monotonically with total volume, i.e., $\widetilde{W}_{net,mm}$ increases approximately as $\widetilde{V}_T^{3/4}$. The optimized external shape aspect ratios are robust with respect to the fuel cell stack total volume, staying approximately within the range $0.03 \leqslant (\xi_y/\xi_x = \xi_z/\xi_x)_{opt} \leqslant 0.07$.

5. Conclusions

In this paper, the constructal optimization of a PEMFC stack was conducted for maximizing the stack net power output. The procedure started with the construction of a mathematical model for fluid flow, mass and heat transfer in a PEMFC stack, which takes into account spatial temperature and pressure gradients in a single PEMFC (Fig. 2), pressure drops in the headers and all gas channels in the entire PEMFC stack (Fig. 3). The single PEMFC internal structure has an optimal allocation, and total thickness being such that wetted area in the reaction layers and electrical resistance are optimally balanced for maximum electrical power, and maximum global stack net power. Additionally, a three-dimensional flow space with the dimensions L_z and L_y in the plane perpendicular to L_x was considered and the total volume was fixed (Fig. 1). The new degrees of freedom, i.e., the aspect ratios L_y/L_x and L_z/L_x, allowed for the optimization of the PEMFC stack external shape, in addition to the single PEMFC internal structure and total thickness. As a result, an external shape was found such that electrical and pumping power are optimally balanced for maximum PEMFC stack net power. Dimensionless optimization results were presented graphically for the sake of generality.

A parametric analysis investigated the effect of stoichiometric ratio, membrane water content, and total PEMFC stack volume on the optima found. For the set of parameters given by Table 1, the optimal PEMFC stack external shape was shown to be "robust" with respect to the analyzed parameters, i.e., $1.5 \leqslant \zeta_1 = \zeta_7 \leqslant 3$, $12 \leqslant \lambda \leqslant 21$, and $0.1 \leqslant \widetilde{V}_T \leqslant 1.16$, and the twice maximized stack net power increases monotonically with total volume, i.e., $\widetilde{W}_{net,mm}$ increases approximately as $\widetilde{V}_T^{3/4}$, similarly to metabolic rate and body size in animals [8]. This is an important finding for the purpose of "scaling up" or "scaling down" PEMFC stack design.

Fundamentally, it was shown that electrical and fluid flow trade-offs exist, and that from them results the single cell internal structure and total thickness, and the PEMFC stack external shape—the relative sizes and spacings—of flow systems, in accordance with other features of constructal design [8,27,28]. In practice, such trade-offs must be pursued based on models that correspond to real applications. The maxima found are sharp, stressing their importance for practical design, and therefore must be identified accurately in the quest for increasing the stack net power efficiency, approaching the actual PEMFC first-law efficiency level. The constructal design results reported in this study demonstrate clearly that in a PEMFC stack, gas supply causes pressure drops that induce considerable power consumption. Those facts need to be taken into account by modeling or experimentally analyzing the entire PEMFC stack, in practical fuel cell design.

Acknowledgements

The authors acknowledge with gratitude the support of NASA under the Hydrogen Research for Florida Universities Program, the Center for Advanced Power Systems at Florida State University, the Brazilian National Council for Scientific and Technological Development, CNPq, and the State of Parana Araucaria Foundation, Curitiba, Brazil.

References

[1] National Energy Technology Laboratory, Fuel Cell Handbook, sixth edition, EG&G Technical Services, Inc., Science Applications International Corporation, DOE/NETL-2002/1179, Morgantown, West Virginia, 2002.
[2] M.M. Mench, C. Wang, S.T. Thynell, An introduction to fuel cells and related transport phenomena, Int. J. Transp. Phenom. 3 (2001) 151–176.
[3] K. Kordesch, G. Simander, Fuel Cells and their Applications, VCH Publishers, New York, 1996, ISBN 3-527-28579-2.
[4] H. Chang, P. Koschany, C. Lim, J. Kim, Materials and processes for light weight and high power density PEM fuel cells, J. New Mater. Electrochem. Syst. 3 (1) (2000) 55–59.
[5] E. Middelman, W. Kout, B. Vogelaar, J. Lenssen, E. de Waal, Bipolar plates for PEM fuel cells, J. Power Sources 118 (1–2) (2003) 44–46.

[6] O.J. Murphy, A. Cisar, E. Clarke, Low-cost light weight high power density PEM fuel cell stack, Electrochim. Acta 43 (24) (1998) 3829–3840.
[7] A. Kumar, R.G. Reddy, Materials and design development for bipolar/end plates in fuel cells, J. Power Sources 129 (1) (2004) 62–67.
[8] A. Bejan, Shape and Structure, from Engineering to Nature, Cambridge University Press, Cambridge, UK, 2000.
[9] T.E. Springer, T.A. Zawodzinski, S. Gottesfeld, Polymer electrolyte fuel cell model, J. Electrochem. Soc. 138 (8) (1991) 2334–2341.
[10] S.F. Baxter, V.S. Battaglia, R.E. White, Methanol fuel cell model: anode, J. Electrochem. Soc. 146 (1999) 437–447.
[11] V. Gurau, F. Barbir, H. Liu, An analytical solution of a half-cell model for PEM fuel cells, J. Electrochem. Soc. 147 (2000) 2468–2477.
[12] A.A. Kulikovsky, J. Divisek, A.A. Kornyshev, Two-dimensional simulation of direct methanol fuel cells—a new (embedded) type of current collector, J. Electrochem. Soc. 147 (2000) 953–959.
[13] T. Thampan, S. Malhotra, H. Tang, R. Datta, Modeling of conductive transport in proton-exchange membranes for fuel cells, J. Electrochem. Soc. 147 (2000) 3242–3250.
[14] L. Pisani, G. Murgia, M. Valentini, B. D'Aguanno, A working model of polymer electrolyte fuel cells—comparisons between theory and experiments, J. Electrochem. Soc. 149 (7) (2002) A898–A904.
[15] S.M. Senn, D. Poulikakos, Tree network channels as fluid distributors constructing double-staircase polymer electrolyte fuel cells, J. Appl. Phys. 96 (1) (2004) 842–852.
[16] T. Zhou, H. Liu, A general three-dimensional model for proton exchange membrane fuel cells, Int. J. Transp. Phenom. 3 (2001) 177–198.
[17] J.C. Amphlett, R.F. Mann, B.A. Peppley, P.R. Roberge, A. Rodrigues, A model predicting transient responses of proton exchange membrane fuel cells, J. Power Sources 61 (1–2) (1996) 183–188.
[18] J. Hamelin, K. Agbossou, A. Laperriere, F. Laurencelle, T.K. Bose, Dynamic behaviour of a PEM fuel cell stack for stationary applications, Int. J. Hydrogen Energy 26 (6) (2001) 625–629.
[19] S.O. Morner, S.A. Klein, Experimental evaluation of the dynamic behavior of an air-breathing fuel cell stack, J. Solar Energy Eng.—Trans. ASME 123 (3) (2001) 225–231.
[20] H.I. Lee, C.H. Lee, T.Y. Oh, S.G. Choi, I.W. Park, K.K. Baek, Development of 1 kW class polymer electrolyte membrane fuel cell power generation system, J. Power Sources 107 (1) (2002) 110–119.
[21] T. Van Nguyen, M.W. Knobbe, A liquid water management strategy for PEM fuel cell stacks, J. Power Sources 114 (1) (2003) 70–79.
[22] M.W. Knobbe, W. He, P.Y. Chong, T.V. Nguyen, Active gas management for PEM fuel cell stacks, J. Power Sources 138 (1–2) (2004) 94–100.
[23] D. Thirumalai, R.E. White, Steady-state operation of a compressor for a proton exchange membrane fuel cell system, J. Appl. Electrochem. 30 (5) (2000) 551–559.
[24] Y.J. Zhang, M.G. Ouyang, Q.C. Lu, J.X. Luo, X.H. Li, A model predicting performance of proton exchange membrane fuel cell stack thermal systems, Appl. Therm. Eng. 24 (4) (2004) 501–513.
[25] J.J. Baschuk, X.G. Li, Modelling of polymer electrolyte membrane fuel cell stacks based on a hydraulic network approach, Int. J. Energy Res. 28 (8) (2004) 697–724.
[26] I. Mohamed, N. Jenkins, Proton exchange membrane (PEM) fuel cell stack configuration using genetic algorithms, J. Power Sources 131 (1–2) (2004) 142–146.
[27] J.V.C. Vargas, A. Bejan, Thermodynamic optimization of internal structure in a fuel cell, Int. J. Energy Res. 28 (4) (2004) 319–339.
[28] J.V.C. Vargas, J.C. Ordonez, A. Bejan, Constructal flow structure for a PEM fuel cell, Int. J. Heat Mass Transfer 47 (19–20) (2004) 4177–4193.
[29] R.B. Bird, W.E. Stewart, E.N. Lightfoot, Transport Phenomena, second ed., Wiley, New York, 2002.
[30] J.S. Newman, Electrochemical Systems, second ed., Prentice Hall, Englewood Cliffs, NJ, 1991, pp. 255, 299, 461.
[31] J.A. Wesselingh, P. Vonk, G. Kraaijeveld, Exploring the Maxwell–Stefan description of ion-exchange, Chem. Eng. J. Biochem. Eng. J. 57 (1995) 75–89.
[32] M.J. Moran, R. Shapiro, Fundamentals of Engineering Thermodynamics, third ed., Wiley, New York, 1993.
[33] W.L. Masterton, C.N. Hurley, Chemistry Principles and Reactions, third ed., Saunders College Publishing, Orlando, FL, 1997.
[34] T.A. Zawodzinski, M. Neeman, L.O. Sillerud, S. Gottesfeld, Determination of water diffusion-coefficients in perfluorosulfonate ionomeric membranes, J. Phys. Chem. 95 (15) (1991) 6040–6044.
[35] J.O'M. Bockris, D.M. Drazic, Electro-chemical Science, Taylor and Francis, London, 1972.
[36] A.J. Bard, L.R. Faulkner, Electrochemical Methods—Fundamentals and Applications, second ed., Wiley, New York, 2001.
[37] G. Li, P.G. Pickup, Ionic conductivity of PEMFC electrodes, J. Electrochem. Soc. 150 (11) (2003) C745–C752.
[38] A.P. Saab, F.H. Garzon, T.A. Zawodzinski, Determination of ionic and electronic resistivities in carbon/polyelectrolyte fuel-cell composite electrodes, J. Electrochem. Soc. 149 (12) (2002) A1541–A1546.
[39] R.K. Shah, A.L. London, Laminar flow forced convection in ducts. Advances in Heat Transfer, Academic Press, New York, 1978. (Suppl. 1).
[40] A. Bejan, Convection Heat Transfer, third ed., Wiley, New York, 2004, Chapter 8.
[41] D.R. Lide (Ed.), CRC Handbook of Chemistry and Physics, 83rd ed., CRC Press, Boca Raton, FL, 2002–2003.
[42] D. Kincaid, W. Cheney, Numerical Analysis Mathematics of Scientific Computing, first ed., Wadsworth, Belmont, CA, 1991.
[43] M.R. Tarasevich, A. Sadkowski, E. Yeager, in: B.E. Convay, J.O'M. Bockris, E. Yeager, S.U.M. Khan, R.E. White (Eds.), Comprehensive Treatise of Electrochemistry, 7, Plenum, New York, 1983, pp. 310–398.